Growth and transfer of graphene and hexagonal boron nitride by chemical vapor deposition : applications to thermally efficient flexible electronics

Théo Levert

To cite this version:

Théo Levert. Growth and transfer of graphene and hexagonal boron nitride by chemical vapor deposition : applications to thermally efficient flexible electronics. Micro and nanotechnologies/Microelectronics. Université de Lille, 2019. English. NNT : 2019LILUI007 . tel-03621668

HAL Id: tel-03621668
https://theses.hal.science/tel-03621668v1
Submitted on 28 Mar 2022

Communauté
d'Universités et d'Établissements
Lille Nord de France

Université
de Lille

THESE

Présentée à l'Université de Lille
Ecole Doctorale Sciences Pour l'Ingénieur

Pour obtenir le grade de :

DOCTEUR DE L'UNIVERSITE

Spécialité : MICRO ET NANO TECHNOLOGIES, ACOUSTIQUE ET TELECOMMUNICATIONS

Par Théo LEVERT

Growth and transfer of graphene and hexagonal boron nitride by chemical vapor deposition. Applications to thermally efficient flexible electronics.

Soutenance le 13 Mars 2019 devant la Commission d'examen

Membres du Jury:

Mr Aziz Benlarbi Delai	Rapporteur (Sorbonne Université – Paris)
Mr Laurent Pichon	Rapporteur (IETR – Université de Rennes)
Mme Christelle Aupetit Berthelemot	Présidente (Xlim – Université de Limoges)
Mme Bérengère Lebental	Examinatrice (IFSTTAR – Université Paris Est)
Mr Henri Happy	Directeur de thèse (IEMN – Université de Lille)
Mr Philippe Coquet	Co-Directeur de thèse (CINTRA – UMI CNRS Singapour)
Mr Emiliano Pallecchi	Co-Encadrant (IEMN – Université de Lille)
Mr Edwin Teo Hang Tong	Co-Encadrant (CINTRA – NTU - UMI CNRS Singapour)

Remerciements

Je ne peux terminer ces trois années et demi de thèse, riches en découvertes et émotions sans procéder à quelques remerciements.

Cette thèse s'est déroulée entre l'IEMN à Lille et CINTRA à Singapour, sous la direction de Henri Happy et Philippe Coquet et sous l'encadrement de Emiliano Pallecchi et Edwin Teo Hang Tong. Je tiens tout d'abord à les remercier chaleureusement pour leur accueil, leurs conseils, leur expertise mais aussi leur relation avec moi durant les différents séjours effectués à Lille ou à Singapour, et de m'avoir offert d'excellentes conditions pour la réalisation de mes travaux.

Je tiens aussi à remercier les membres de mon jury, à savoir Mme la Présidente Christelle Aupetit-Berthelemot de l'université de Limoges, les rapporteurs Aziz Benlarbi-Delai de Sorbonne université et Laurent Pichon de l'université de Rennes, ainsi que Bérengère Lebental de l'université Paris Est, examinatrice. Ils ont su lire mon travail, le juger et me questionner pertinemment sur ces travaux.

Je tiens aussi à remercier les personnes avec qui j'ai pu collaborer durant ces travaux, à savoir les membres de l'équipe techno, notamment Elisabeth Galopin, Pascal Tilmant, François Vaurette et tous les autres pour leurs conseils sur les différentes étapes technologiques. Un remerciement tout particulier à Dominique Vignaud avec qui j'ai pu travailler étroitement sur l'aspect matériau et son aide pour la spectroscopie Raman. Je remercie aussi Tous les autres membres de l'équipe CARBON avec qui j'ai pu travailler, à savoir Emmanuelle Pichonat, Wei Wei, Soukaina Bensalk et Dalal Fadil.

Un gros merci aux personnes de l'équipe CINTRA qui m'ont épaulé et permis de m'intégrer facilement dans la vie du laboratoire et plus généralement dans la vie singapourienne, à savoir Ange, Nicolas, Mathieu, Etienne, Holger et les autres.

Un gros merci, comme le dit Charles Aznavour à « mes amis, mes amours, mes emmerdes », qui seraient un peu trop long à citer ici. Je remercie quand même toute la team Picardie, avec qui nos liens d'amitiés perdurent dans le temps, ainsi que mes nouveaux amis lillois. Je tiens tout particulièrement à remercier le Uno's bar pour m'avoir permis de décompresser les nombreux soirs où c'était nécessaire, autour d'une bière et d'une partie de Ping-Pong, m'ayant permis de faire des rencontres incroyables.

Je tiens à remercier aussi mes colocs incroyables Pilou, Léo et Jordane qui m’auront permis durant cette quasi dernière année de retrouver un chez nous, non pas désert comme le dit Aznavour, mais rempli de vie et d’amour, au rythme des barbecues et soirées musiques.

Enfin je tiens à remercier mes parents et ma famille qui m’auront soutenu (et surtout supporté) durant ces années.

Table of content

General Introduction

As the fourth most abundant element in the universe, Carbon plays an important role in the emerging of life in earth as we know it today. The industrial era has seen this element at the heart of technological applications due to the different ways in which carbon forms chemical bonds, giving rise to a series of allotropes each with extraordinary physical properties. For instance, the most thermodynamically stable allotrope of carbon, graphite crystal, is known to be a very good electrical conductor, while diamond very appreciated for its hardness and thermal conductivity is nevertheless considered as an electrical insulator due to different crystallographic structure compared to graphite. The advances in scientific research have shown that crystallographic considerations are not the only determining factor for such a variety in the physical properties of carbon-based structures. Recent years have seen the emergence of new allotropes of carbon structures that are stable at ambient conditions but with reduced dimensionality, resulting in largely different properties compared to the three-dimensional structures. These new classes of carbon allotropes are namely: carbon nanotubes (one dimensional), fullerene (zero dimensional), and the last discovered allotrope of carbon, also known as the first two-dimensional material: graphene

Graphene, a 2D material consisting of a monolayer of carbon atoms forming a honeycomb structure, is well known for its unique properties, such as electronic, mechanic and thermal properties[1],[2],[3],[4]. Its electronic band structure does not have a forbidden band, making it a zero-gap semiconductor. Moreover the electronic mobility of charge carriers is very high compared to other materials[5]. This material has also a high thermal conductivity[6] and an ability to stand great deformations[7]. Thus, it is a good candidate for many applications.

Wallace has first studied band structure and other properties of graphene theoretically in 1947[8]. However, the technical limitations did not permit to study its properties experimentally at this time. We had to wait until 2004 for the work of Geim and Novoselov who first succeed to isolate a monolayer of graphene from the exfoliation of graphite[9], which gave them the Nobel prize in 2010. Since then, many scientists focused on graphene with both theoretical and experimental studies. In 2013 a European project “Graphene Flagship” was launched for a duration of 10 years. The Carbon group at IEMN is involved in the project since its inception.

For more than 10 years, other 2D materials appeared such as transition metal dichalcogenides or hexagonal boron nitride (h-BN). They have complementary properties and a great potential for many applications. h-BN is a wide gap semiconductor with a similar structure as graphene, with a honeycomb lattice which named it commonly as “white graphene”, with similar mechanical and thermal properties[10].

A major challenge is to find a way to grow those materials in order to achieve an easy and economically attractive way to produce large area of those materials with a good quality. Another challenge is to transfer those materials on substrate compatible with electronics (mainly SiO_2), or the realization of heterostructures of such materials. We will focus in this first part of our work on investigation of the growth conditions required to produce large area graphene (few centimeters) and h-BN of good quality and their transfer on SiO_2.

Flexible electronics has become an important field of research for many applications, such as flexible batteries[11], RFID tags[12], displays[13] or touch screens[14]. In this goal, several materials have been used such as PEN, PET or polyimide (PI). All these materials present a good flexibility and a chemical compatibility with microelectronics process but they suffer from poor thermal conductivity, leading to lower utilization of power of devices deposited compared to classic microelectronic substrate such as SiO_2. Several ways have been recently investigated to bypass this problem and a good solution is to fill the matrix of the polymer or polyimide with nanomaterials or nanofillers. We choose to use graphene and h-BN as the filler in a 3D shape: a foam of graphene or h-BN as the nanofiller and we chose a PI as the matrix. In this second part, we will explain in detail how we achieve novel flexible substrates with enhanced thermal properties.

Chapter 1: Growth, transfer and characterization of graphene and h-BN

I) Introduction

I.1) Objectives

Graphene and h-BN are unique materials due to their form as monoatomic layers. Their synthesis by CVD process can be seen as the deposition of a very thin film through the pyrolysis of a gas precursor. As a result, we can adapt the growth model used in the thin film deposition model for the CVD growth. We can then understand how the process parameters such as pressure, temperature or gas flow can affect the morphology of the resulting materials, helping us preparing some large area graphene (few cm²) and h-BN with properties closer of those achieved in mechanically exfoliated graphene and h-BN.

As CVD graphene and h-BN are monoatomic layers growing on metallic substrates, they require the use of a supporting layer in order to be transferred onto a target substrate. This supporting layer requires mechanical robustness and handling convenience. In this part, I will describe the technique developed for the transfer of 2D materials on the suitable substrate.

Another objective of this work is to grow graphene and h-BN as 3D material (thick). The objective is to exploit the thermal properties of 2D material, for heat dissipation in the circuits. We decided to grow 3D graphene and h-BN structures as a foam in order to obtain thick materials. This is particularly important for applications in flexible electronics, where heat dissipation remains a major issue.

I.2) Graphene

Graphene has been studied theoretically as based material of graphite since the 40’s. The first work on electronic properties of a 2D material have been published in 1947[8]. In 2004 Novoselov and Geim showed for the first time the stability of few layers of graphene and studied their electronic transport properties[9]. Those studies opened the way of the development of new technologies based on the outstanding properties of this material. Since then, the number of publications on graphene increased significantly, as we can see on Figure 1:

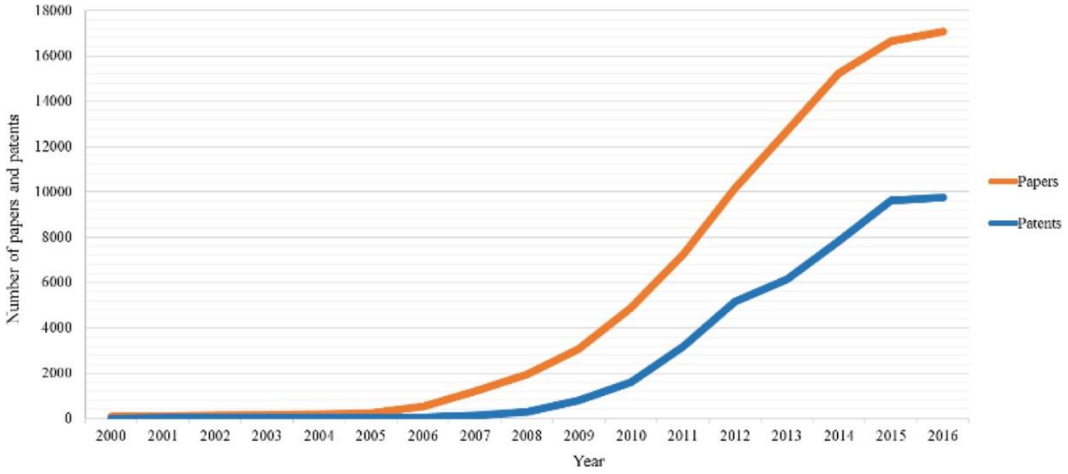

Figure 1: Number of publications and patents on graphene from 2000 to 2016[15]

Graphene is one of the allotropes of carbon. It is defined as a 2D monolayer of carbon placed as a honeycomb lattice, following a hexagonal network. We can see in the Figure 2 a periodicity in the crystallographic structure when considering a unit cell composed of two neighbor atoms of carbon (A and B). Two vectors $\overrightarrow{a_1}$ and $\overrightarrow{a_2}$ define each of the unit cells:

$$\overrightarrow{a_1} = \frac{a_{CC}}{2}\left(3, \sqrt{3}\right), \overrightarrow{a_2} = \frac{a_{CC}}{2}\left(3, -\sqrt{3}\right)$$

With $a_{CC} = 1.42\text{Å}$, corresponding to the distance between two neighbor carbon atoms.

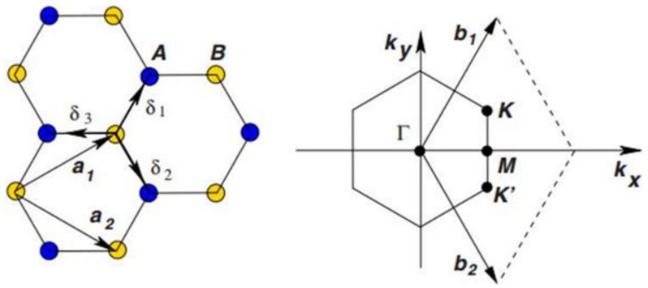

Figure 2: Representation of the graphene structure in (a) real space and (b) reciprocal space[1]

From those two vectors, two other vectors of the reciprocal space $\overrightarrow{b_1}$ and $\overrightarrow{b_2}$ are defined as:

$$\overrightarrow{b_1} = \frac{2\pi}{3a_{CC}}\left(1, \sqrt{3}\right), \overrightarrow{b_2} = \frac{2\pi}{3a_{CC}}\left(1, -\sqrt{3}\right)$$

From the unit cell of the reciprocal space, the Brillouin zone can be obtained. In the reciprocal space, two points are important: The K and K' points also called Dirac points.

The electronic configuration of a carbon atom is $1s^2 2s^2 2p^2$. There is in total six electrons whose two of the 1s orbital are the closest to the nucleus and are bonded. The four valence electrons of the two external orbitals allows it to form covalent bonds of the type σ and π. By using the tight-blinding approximation for graphene, it can be shown that a carbon atom is bonded with its 3 neighbors by σ bonds from the recovery of sp^2 orbitals, formed by the hybridization of atomic orbital 2s and of the two orbitals 2p included in the graphene plane. In addition to those bonds, each atom of carbon has an electron in the p_z orbital perpendicularly to the graphene plane. Those π electrons are very movable and they are the main actors of the transport properties of graphene. The great difference of energy (10eV) of the bonding and anti-bonding orbital σ makes the σ electrons not playing a role in the electronic and optical properties of graphene[16]. Considering the hopping of only nearest neighbors and one π orbital per atom, we can use a tight-binding Hamiltonian to describe the band structure of graphene. Considering an undoped graphene, the valence and conduction bands meet at the Dirac points K and K', making it a zero-gap semiconductor. At the Dirac point, for low energies, the energy-movement relation is linear as we can see in Figure 3, making electrons in this situation called Dirac fermions, with the particularity to have a zero effective mass[1].

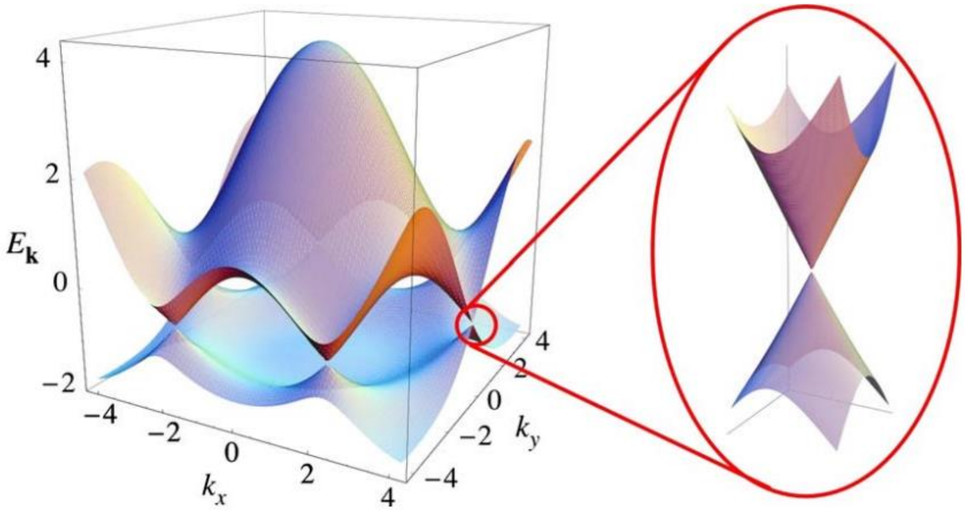

Figure 3: Electronic dispersion in the honeycomb lattice. Left: energy spectrum. Right: zoom in of the energy bands close to one of the Dirac points[1].

Graphene has also other unique properties. First its mechanical properties are impressive due to its thickness and its flexibility, but also due to its mechanical resistance (Young modulus of 0.5TPa[17]) because of the hybridization of sp^2 orbitals, making it a material of choice for flexible electronics. Moreover it has interesting optical properties with a high transparency (absorption of 2.3% of visible light for a monolayer[18]). It is also a good thermal conductor, with a thermal conductivity up to 5000W.m^{-1}.K^{-1}[6] at room temperature.

Characteristics	Parameter	Value
Mechanical	Young modulus	0.5TPa
	Compression Resistance	300-560MPa
Thermal	Specific heat @25°C	$700 J.K^{-1}.kg^{-1}$
	Thermal conductivity @20°C	$2000\text{-}5000\ W.m^{-1}.K^{-1}$
	Sublimation point	4240°C
Electrical	Bandgap	0eV
	Mobility	Up to 200000 $cm^2V^{-1}s^{-1}$

Table 1: Major properties of graphene

I.3) h-BN

Boron nitride is a III-V material. Unless other III-N nitride materials, which most stable structure is wurtzite, BN has four stable structure: hexagonal BN (h-BN), cubic BN (cBN), wurtzite BN (wBN) and rhomboedral BN (rBN). The hexagonal structure is stable at room temperature, the cubic structure is stable at high temperature and the two others are metastable at high pressure. We will focus in this work on h-BN, due to its 2D nature and outstanding properties.

Boron nitride is not a natural material. Its first synthesis was made in 1842 by Balmain[19], using the reaction of boric acid melted on potassium cyanide. Unfortunately, the material was very unstable, and researchers used hundred years before finding a stable phase as powder. Bore (Z=5) and nitrogen (Z=7) are situated around carbon (Z=6) in the periodic classification, BN and carbon materials have similar stable structures: h-BN has a similar structure to graphite and cBN has a similar structure to diamond. Table 2 shows the different parameters of lattices.

	h-BN	graphite	**cBN**	diamond	**wBN**	**rBN**
Parameters of lattice (nm)	**a=0.25038** **c=0.661**	a=0.2464 c=0.6738	**a=0.3615**	a=0.357	**a=0.2536** **c=0.4199**	**a=0.2504** **c=1.002**
Closest atom distance (nm)	**0.1446**	0.142	**0.1565**	0.154	**0.1555**	**0.145**

Table 2: Lattice parameters of the different allotropes of BN and carbon

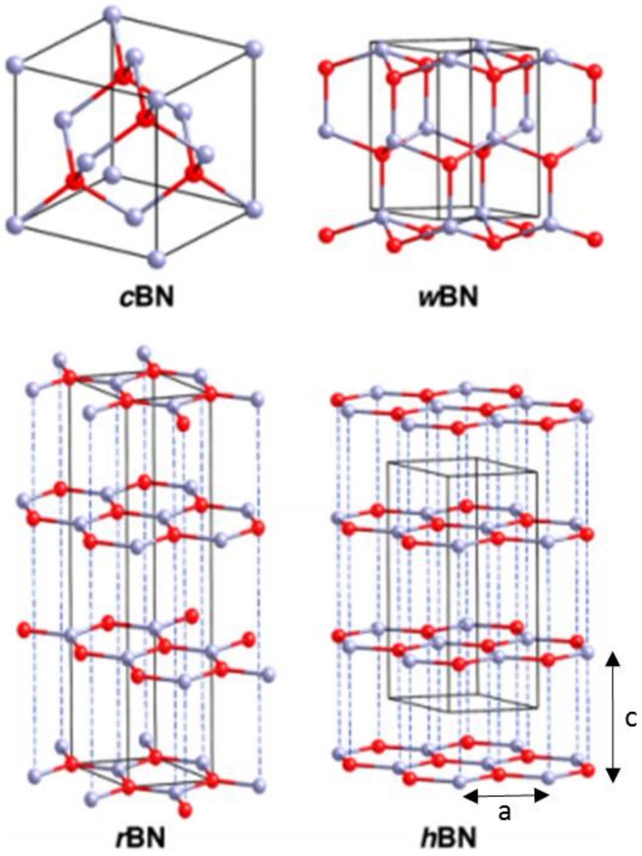

Figure 4: Structure of c-BN, w-BN, r-BN and h-BN[20]

h-BN phase is very similar to graphite with close lattice parameters (a=0.2464nm and c=0.6738nm for graphite). Its structure is formed by sheets stacked with an ABAB type. However, the difference of chemical nature of B and N atoms in the plane make the stack atoms perfectly on atoms (contrary to graphite) alternately with B and N. The force between the different sheets is a Van der Waals type. The distance between two planes is 3.3Å and the hexagons in the different sheets are made by BN covalent bonds with a distance of 1.45Å with a sp^2 hybridization. The force of the covalent bond in the plane is much higher than the Van der Waals force between the sheets, giving at this material its peculiar properties.

h-BN is a nontoxic material. We can use it at high temperature (850-900°C if presence of oxidation), which is quite higher than graphite (oxidation at 600°C. Moreover, it is transparent for visible light, making it a material of choice for transparent electronics. Its main physical properties are very close to graphene's one, with a high mechanical robustness, a good thermal conductivity. However, h-BN is a semiconductor with a wide bandgap (5-6eV), making it a good substrate for electronics. Some theoretical studies on electronic properties of h-BN showed that its bandgap is first-order independent of the details of the atomic structure. Its dimensions are really close to the one of graphene (mismatch around 1.7%). Thus, many studies interested in the realization of heterostructures such as graphene/h-BN or sandwiches h-BN/graphene/h-BN for the realization of graphene field effect transistors (GFETs) or graphene/h-BN/graphene for the realization of tunneling field effect transistors. It must be noticed that h-BN, as well as graphene has a good thermal conductivity, which is a very important point for our work. Most physical properties of h-BN are presented in Table 3:

Characteristics	Parameter	**Value (h-BN)**	Value (graphene)
Mechanical	Young modulus	**0.7-1TPa**	0.5TPa
	Compression Resistance	**30-120MPa**	300-560MPa
Thermal	Specific heat @25°C	**800-2000J.K^{-1}.kg^{-1}**	700J.K^{-1}.kg^{-1}
	Thermal conductivity @20°C	**1700-2000W.m^{-1}.K^{-1}**	2000-5000 W.m^{-1}.K^{-1}
	Sublimation point	**2600-2800°C**	4240°C
Electrical	Static dielectric constant	**7.04(⊥)-5.09(//)**	
	High frequency dielectric constant	**4.95(⊥)-4.1(//)**	
	Bandgap	**4.97eV**	0eV

Table 3: Principal physical properties of h-BN and graphene[21]

II) Growth and transfer of 2D graphene

1) CVD growth of graphene

The CVD growth of graphene depends mainly on two things: a catalyst, which is in most case a transition metal such as Cu, Ni, Pt, Co, Au, Fe, Ru, Ir, Pd… and a precursor, which corresponds to the source of carbon forming the graphene on the catalyst. The catalysts mainly used are methane, ethylene or benzene.

The total procedure of the graphene growth of graphene by CVD is always the same for every catalyst, namely a heating step, an annealing of the catalyst, then the growth step with the injection of the precursors at a constant temperature, then a cooling step down to room temperature. The Figure 5 shows a schematic of these four steps

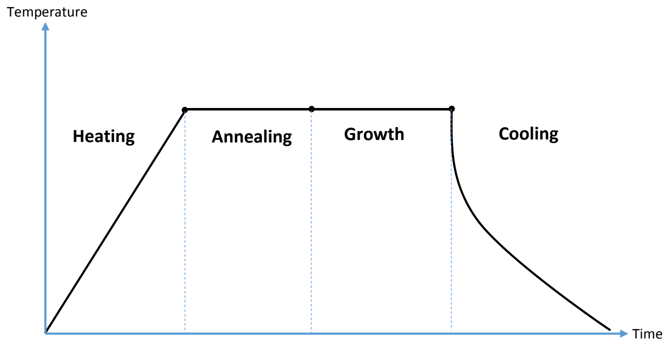

Figure 5: Schematic of the four steps of a CVD growth of graphene

Table 4: Carbon solubility and the growth mechanism on typical metals for CVD graphene:

Metal	Carbon solubility at 1000 °C (at.%)[22]	Growth mechanism
Cu	0.04	Surface deposition/Penetration
Co	3.41	Segregation
Pt	1.76	Segregation/Surface deposition
Ni	2.03	Segregation/Surface deposition

The growth mechanisms of graphene are depending on the catalyst, the precursor and the growth conditions. It is especially the solubility of the precursor which is the main factor. If the transition metal has a high carbon solubility (such as Ni), then after the growth and before the cooling there will be graphene at the surface of the metal, but also some carbon dissolved in the bulk material. When the temperature decreases, the carbon atoms dissolve in the metal will be evacuated and reached the surface of the metal, forming substantial layers of graphene. As a result, it is more complicated to obtain a monolayer of graphene with metals with a high carbon solubility such as Ni than a metal with a low carbon solubility such as Cu. Table 4 shows the solubility of few transition metals.

The growth mechanism determines the interaction between the graphene and the catalyst. Batzill et al.[23] showed that there are three different mechanisms: Surface deposition, penetration and segregation. Table 4 shows the different mechanisms involved for some transition metals used. It must be noticed that these growth mechanisms are also depending on the temperature. We will concentrate on the growth of graphene on Cu and Ni, which are the two metals used in this work.

The main advantage of the Cu as a catalyst is its low solubility of carbon. Indeed the Cu is not a carbon “tank” after the growth, so very few carbon atoms will segregate at the Cu surface during the cooling, making it a good candidate for the growth of graphene monolayer[24]. However, it is less reactive than Ni and it requires temperature around

1000°C to observe dissociation of the precursor at its surface, which is close to the sublimation temperature of Cu. Thus, it is very important to have a good control of the growth in order to avoid the sublimation of the copper foil in the CVD system. The growth principle of graphene on copper is a heating up to the growth temperature under a H_2 flow, in order to increase the size of the Cu grains (which can be as big as 2mm under low pressure). Once the growth temperature reached, we insert the precursor in the CVD system, which will dissociate on the surface of the copper foil, leading into a saturation in carbon at the surface of the copper foil. As a result, we can observe the nucleation of graphene on the surface of the copper foil and an expansion of the graphene domains until they reach each other. Thereby we obtain a continuous layer of graphene, electrically continuous but with several domains, with the possibility of different orientations of the domains. Then we perform the cooling down to the room temperature. In most of the case the growth of graphene on copper leads to the formation of a monolayer due to the reasons explained previously, but in bad growth conditions (flow of the precursor to high or growth time too long) we can observe the formation of multilayers at the nucleation spots.

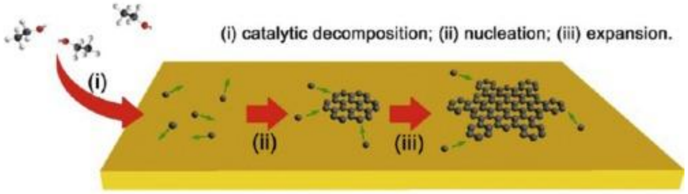

Figure 6: Schematic of the CVD growth of graphene on copper[25]

Ni as a catalyst has not been studied as much as the copper because the control of the number of layers and the uniformity of the growth is really hard because of the high solubility of carbon in nickel. However Nickel is still a good candidate for the graphene growth because the dissociation of the precursor occurs at lower temperature[26]. The growth of graphene on nickel consists on an increase of the temperature up to the temperature growth under a H_2 flow in order to increase the size of the nickel grains[27]. When the growth temperature is reached, we insert the precursor into the CVD system. First the carbon dissolves into the nickel and then nucleation spots appeared at the surface of the nickel and the graphene growth begins. After some time, we stop the precursor exposure and we start the cooling. During this cooling, depending on the growth temperature and the temperature rate, we can observe the segregation of the carbon inside the Ni at the surface, leading to the formation of multilayers of graphene at the surface.

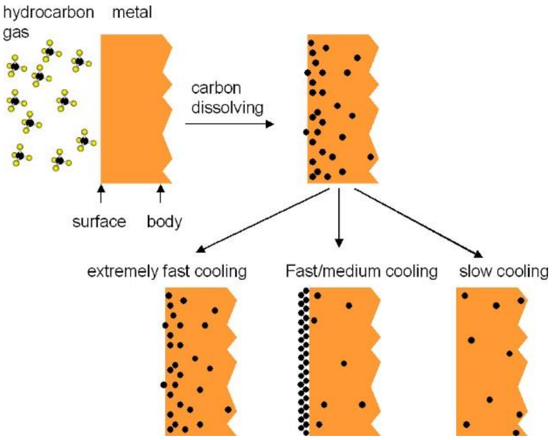

Figure 7: Schematic of the CVD growth of graphene on nickel[28]

2) Characterization of graphene

The quality of graphene varies depending on the growth parameters, the choice of the precursor or the catalyst. Thus, it is important to systemically control the quality of graphene to validate or not the growth conditions. Several techniques have been developed and adapted for graphene. For our work we focused on 3 main characterization techniques: Optical microscopy, scanning electron microscopy (SEM) and Raman spectroscopy.

a) Optical microscopy

Optical microscopy is a good way to observe graphene. Indeed, the association of an optical microscope with a specificity of the substrate allows a good and quick identification of graphene. In this work we chose to transfer graphene onto SiO_2/Si substrates. The optical contrast results from light interferences inside the SiO_2. The thin oxide layer acts as a Fabry Perrot cavity. The transfer of graphene on such substrates for specific SiO_2 thickness increases the optical contrast and allows us to identify the graphene with this simple method[29]. The following figure shows the optical contrast as a function of the wavelength and the SiO_2 thickness.

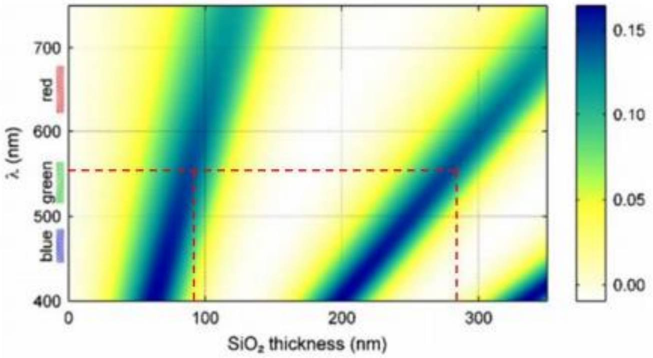

Figure 8: Optical contrast of graphene as a function of the wavelength and the SiO_2 thickness[29]

We can see that the optical contrast of graphene is at his maximum at thickness of SiO_2 of 90 and 285nm for a 55nm wavelength (which corresponds to the maximum of sensibility of human eyes). Thus, we chose to work with substrate with a thickness of SiO_2 at around 280-300nm. The observation of transferred samples with optical microscopy allows us to confirm its presence but also to evaluate quickly its quality, with the formation for example of holes or cracks during the transfer. Figure 9 shows an example of graphene transferred onto SiO_2.

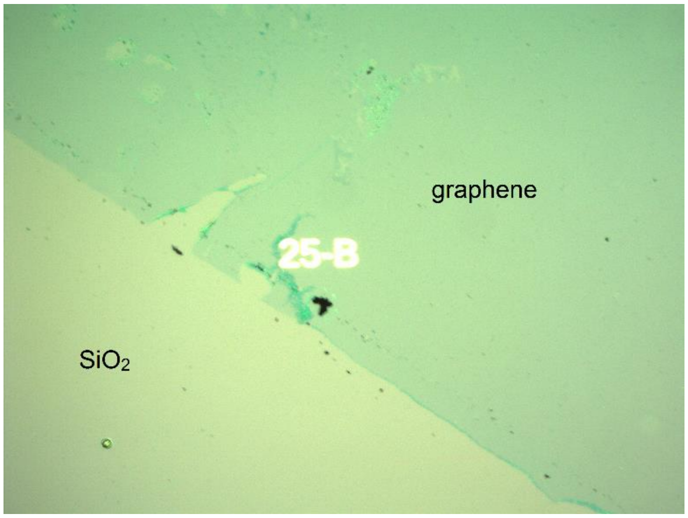

Figure 9: Example of optical image of graphene on SiO_2

However, this technique does not help for the identification of the number of layers of graphene or the crystallinity quality of graphene, letting us use other technique such as SEM, AFM and Raman spectroscopy.

b) Scanning Electron Microscopy

Scanning electron microscopy (SEM) is a quick and nondestructive technique to observe samples at high magnification. It is based and electron-material interaction. The principle of SEM is based on a scan of a sample with an electron beam and the detection of back electrons point by point, in order to create a cartography of all the scanned surface. The secondary electrons coming on the detector are coming from a zone at around 10nm on the surface of the sample and are really sensitive to the topography. The lateral resolution is close to the diameter of the electron beam (few nm), resulting in high magnification of the collected images. SEM is an important tool for morphological characterization and has no constraint concerning the size of the sample.

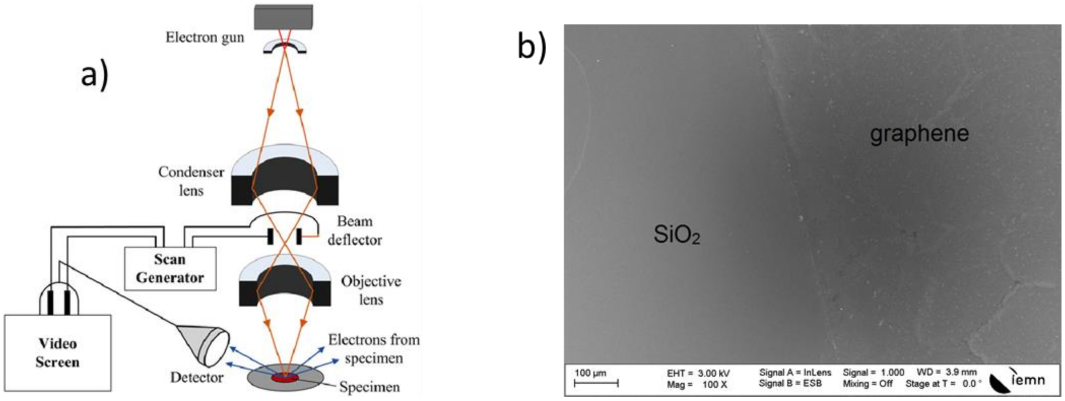

Figure 10: a) Schematic diagram of the SEM working principle[30] and b) SEM image of graphene on SiO_2

c) Raman spectroscopy

Raman spectroscopy is a non-destructive characterization technique, which is a great advantage for the study of graphene. Moreover, it is a technique pretty fast to use and requires no preparation of the sample. This technique has been discovered in 1928 by Chandrasekhar Raman[31] and is based on the interaction of the inelastic scattering of a monochromatic light and the molecular vibrations of the studied material (i.e photon-phonon interaction).

The principle consists of focalizing a monochromatic light source (usually from a laser) and to analyze the diffused light. Indeed, the material is set at a virtual level of energy by the scattering of the coming photons. The material emits back the photons with a different energy level. This back scattering shows two types of signals:

- Rayleigh scattering which is an inelastic scattering of the coming photons without a change of energy level.
- Stokes scattering (or anti-Stokes scattering) in the case where the coming photons interact with the phonons of the studied material with respectively a gain or a loss of energy level. The observed variation of energy gives us the levels of energy of rotation and vibration of the molecules of the studied material.

This energy variation is analyzed by a photodetector. It is called Raman shift. A Raman spectrum shows the diffused Raman intensity as a function of the frequency difference of the coming and the back scattering: if we study the Stokes scattering, this difference is positive and zero for the Rayleigh scattering. For practical reasons, this frequency difference is converted in wavenumber $\bar{\nu}$ by the following formula:

$$\bar{\nu} = \frac{1}{\lambda} = \frac{\nu}{c}$$

With $\bar{\nu}$: wavenumber (in cm^{-1}), λ : wavelength of the scattering (in cm), ν : frequency of the scattering (in Hz) and c : speed of light in vacuum.

Utilization of Raman spectroscopy for carbon materials is not new[32] and especially for graphene[33]. Raman spectrum of graphene are composed of 3 main peaks: G, D and 2D peaks, which can be seen in Figure 11

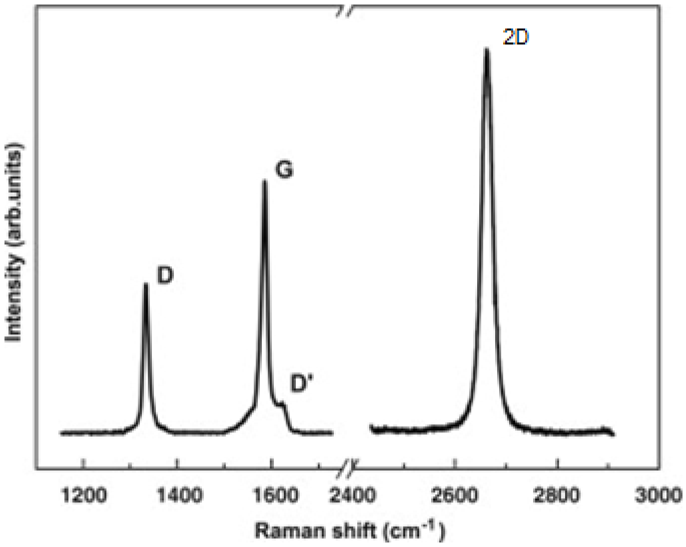

Figure 11: Example of Raman spectra of graphene[34]

- G peak (around 1590cm^{-1}): It is a characteristic signal of graphene and is associated with planar vibrations of sp^2 carbon atoms. It corresponds to a Raman process of 1st order. It results from the phonons of E$_{2g}$ symmetry, which is associated to a shear stress in the unit cell plane.
- 2D or G’ peak (around 2700cm^{-1}): it corresponds to a Raman process of 2nd order. In this configuration, there is a scattering of two phonons: one resulting from the electron scattering excited from a band close to the K point to a band close to the

K’ point, and another one by the same process but on the other side. It corresponds to an intra-valley process.

- D peak (around 1350cm^{-1}): it is a characteristic of the defects or disorder in the graphene plane, and is associated to out-of-plane vibrations. It corresponds to a Raman process of 2nd order with a phonon with a E_{2g} symmetry and a defect of the system necessary for the activation of the D peak[35]. It comes from an elastic scattering of an excited electron from a band close to the K point to a band close to the K’ point on a defect, then a second scattering results in the emission of a photon. This peak is very weak or not present for a high quality graphene[36].

Two other peaks can also be detected: D’ peak and D+G peak:

- D+G peak (around 2940cm^{-1}): This peak corresponds to a process with two phonons and a defect. It is a configuration where the scattering of the D and G peak scattering occur. In that case there is first an elastic scattering from a defect from a band close to the K point to a band close to the K’ point, and a 2nd inelastic scattering with a phonon emission.
- D’ peak (around 1635cm^{-1}): This peak is resulting from an inelastic scattering from an excited electron because of a defect with a phonon emission.
-

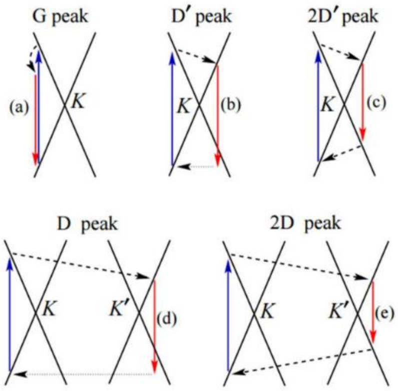

Figure 12: Representation of the different Raman processes resulting in G peak(a), D' peak(b), 2D' peak(c), D peak(d) and 2D peak (e). Blue arrows are corresponding to the absorption of a photon by an electron. Red arrows correspond to the de-excitaion of an electron with a photon emission. Dotted horizontal lines represent an elastic scattering because of a defect and dotted arrows correspond to a scattering process[35]

Thus, the study of Raman spectrum of graphene (Figure 11) can inform us on the quality of the graphene (presence of defects), the number of layers, the doping level… Indeed, the Intensity ratio of some peaks allows us to determine the number of layers or to quantify the defects in graphene. For the number of defects in graphene, the intensity of D peak (I_D) (characteristic for the defects) relatively to the G peak (I_G) is relevant. A low ration I_D/I_G informs us on the low disorder in the graphene plane and so a good crystalline quality of the graphene. When working with a monolayer, one can observe the presence of a 2D peak very sharp and more intense than the G peak. When the number of layers increases, the 2D peak broadens itself and becomes less intense. Thus the ratio of intensity of G peak and 2D peak can informs us on the number of layers[37]. An intensity of the peak 2D 2 to 3 times higher than the intensity of the G peak informs us on the presence of a monolayer. This ratio is equal to 1 in the bilayer case and is superior to 1 over 2 layers. This method is quite simple to determine the number of layers of graphene.

3) Growth of 2D polycrystalline graphene

As discussed earlier, we chose to focus on the growth of graphene using CVD, which is the better way to produce large area graphene for industry. We chose to use commercial Cu foil from Alpha Aesar of high purity (99,9999%) in order to obtain monolayer graphene, as discussed before. Graphene growth has been carried out in a Jipelec JetFirst Rapid Thermal CVD (RTCVD). This system allows heating and cooling at high rates (10°C/s). Heating is provided by halogen lamps on the top of the chamber and the sample placed horizontally onto a Si wafer. The temperature is measured by a thermocouple contacting the sample's back face. The growth itself is decomposed as a heating, an annealing, a growth and a cooling. We used a mixture of 100sccm of Argon and 5sccm of Dihydrogen during all the steps and 20scccm of methane as a precursor during the growth phase. We can see a schematic of the steps in Figure 14. Note that the growth parameters have been optimized by postdoc Geeta.

Figure 13: View of the CVD used for the growth of graphene

We first cut the Cu foil in small pieces (2.5x2.5cm), clean them with acetic acid for 5min, acetone for 5min and IPA for 5min under ultrasound in order to remove all possible copper oxide and to have the cleanest surface possible. We then put the pieces onto a Si wafer in the chamber. We proceed to a high vacuum (<5.10^{-5} bar) before starting and then we start the heating for 5min from room temperature to 300°C and then 2min from 300 to 1070°C, then the annealing for 5min, we continue with the growth for 5min and we finish with a quick cooling of the chamber using a water flow (with a decrease rate of 60°C/s from 1000 to 700°C), then around 10 min to reach room temperature.

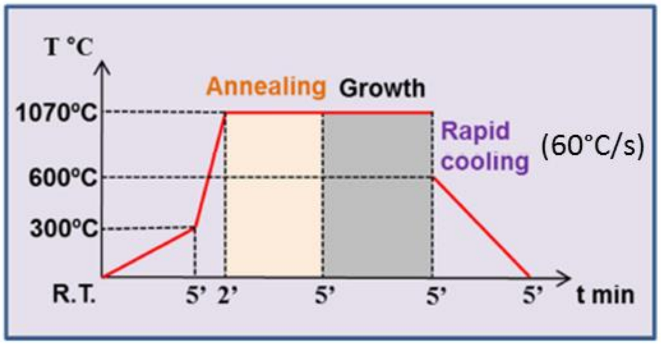

Figure 14: Schematics of the growth parameters

4) Characterization of the grown graphene

An optical image of the as-grown graphene can be seen in Figure 15. The dark lines are the Cu grain boundaries. It can be seen that no grain boundaries of graphene can be seen, indicating that we obtained a full covered sample. No particles or copper oxide have been observed on our samples, indicating a good quality of the copper foil and a good cleaning of the surface before the growth.

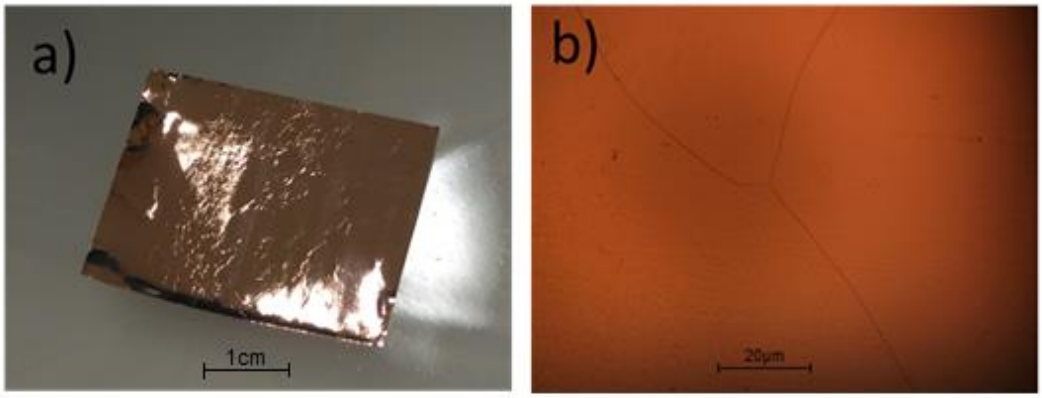

Figure 15: a) Photography and b) Optical image of graphene on Cu

SEM images have been performed using a Zeiss Ultra 55.

The SEM images at low and higher magnification are also indicating that we have a full covered sample, confirming the growth conditions. We can also notice the presence of few nanoparticles on some points of the Cu foil, which surely comes from the quality of the Cu foil, or the cleaning of the foil.

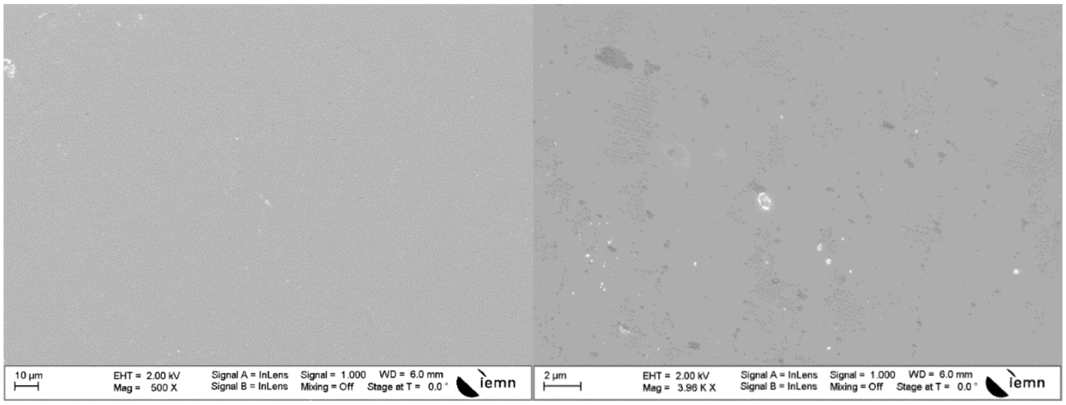

Figure 16: SEM images of graphene on copper foil

However, at higher magnification, at some areas of the surface, we noticed some darker area, indicating the presence of multilayer graphene at the nucleation points, as explained earlier concerning the formation of graphene on copper foil. Nevertheless, the objective of obtaining graphene on all available surface is achieved with these growth conditions, letting us work with large area graphene (3x3cm).

Raman spectroscopy has been carried out using a LabRAM HR Horiba Jobin-Yvon with a 473nm laser as the light source, as we can see in Figure 17:

Figure 17: Photography of the Raman system used in this work

Raman has been performed on the as-grown sample. We can clearly identify the G and 2D peaks at respectively 1581 and 2712cm^{-1} for a FWHM of 29 and 45cm^{-1}, and a weak D peak at 1355cm^{-1}, indicating a high quality graphene. The relative intensities of the G and 2D peak is around 2.1, which is really close to 2, indicating the presence of monolayer graphene. One can notice that we obtained similar spectrum on all available surface of the copper foil, making the sample very homogeneous.

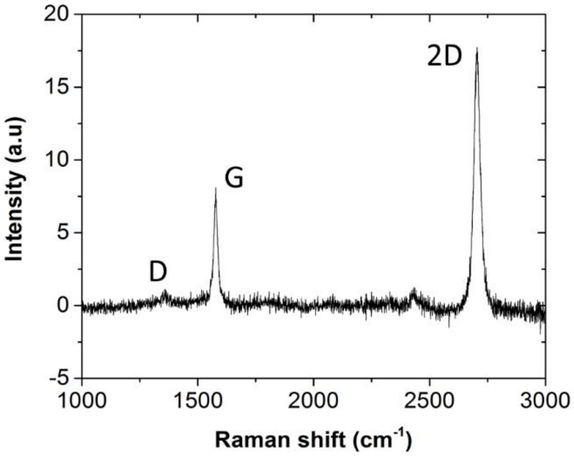

Figure 18: Raman spectra of graphene on copper foil

Thus, we showed that we obtained the good conditions to achieve full covered pieces of copper foil with monolayer graphene of good quality.

5) Transfer of 2D graphene

a) Method of transfer

Various transfer methods are currently developed to prepare graphene onto dielectric substrates for device fabrication. One way to reach this goal is to cover the graphene with a polymer supporting layer (PMMA, for example) to prevent graphene from collapsing, and then etch the underneath Cu foil. Besides increasing visibility and facilitating the handling, the supporting layer is also necessary as bare graphene may collapse due to surface tension.

The wet transfer technique consists on several steps which have been compiled according to what have been done in literature. We first cover the graphene/Cu foil with PMMA and we then perform an annealing at 110°C with a very slow heating and cooling in order to prevent cracks in the graphene due to the difference of the thermal expansion coefficient between copper and graphene. Then we perform an etching of the back graphene at the bottom of the copper foil using an O_2 plasma[38]. The next step is to etch the copper foil. In that aim we use a solution of ammonium persulfate ($(NH_4)_2S_2O_8$), known as a good and clean etchant of copper and copper oxide nanoparticles residues[39] with a concentration of ~200mol.L^{-1} (see appendix for details). We let the PMMA/graphene/Cu float on the surface of the solution. We let the copper being etched for several hours (up to 15h) and we take the floating PMMA/graphene to put it in a DI solution. We repeat this operation around 10 time in order to rinse the graphene from the etchant solution. We can then use a SiO_2 wafer to collect the PMMA/graphene on the top of its surface, by placing the Si wafer at the bottom of the container and removing the remaining water with a pipette until the PMMA/graphene reach the surface of the wafer. We perform again an annealing at 90°C with a slow heating and cooling in order to evaporate all water remaining. For the PMMA removal we first expose our sample to deep UV to facilitate the removal[40]. We then put our sample in different baths of acetone then IPA to remove the PMMA. A schematic of the wet transfer can be found in Figure 19, and the detailed parameters of each step can be found in Annex.I.

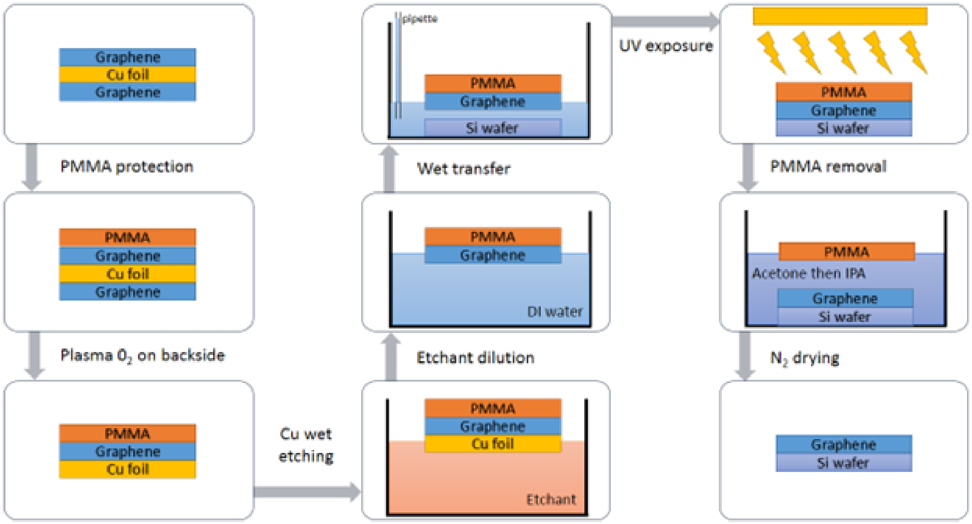

Figure 19: Schematic of the wet transfer technique used in this work

b) Characterization of transferred graphene

The wet transfer process described earlier has been used on our sample in order to achieve a clean transfer of graphene. Figure 20 shows graphene coated with PMMA transferred onto SiO_2 before the removal of the PMMA. We can see that the graphene finds itself very flat on the Si wafer, with absence of bubbles or cracks.

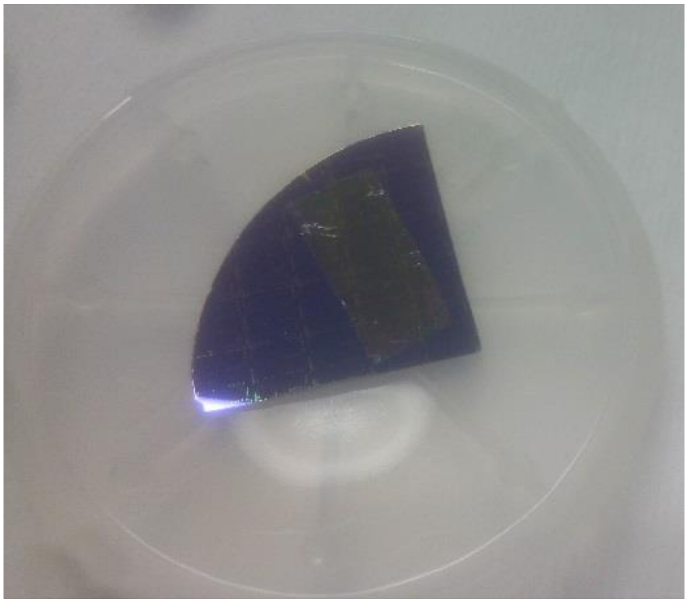

Figure 20: Optical image of graphene with PMMA transferred on SiO_2/Si

After the transfer of graphene, our sample have been slowly annealed, and then we proceeded to the PMMA removal, according to our process. Then it is possible to observe the transferred graphene using an optical microscope, according to the reasons discussed in a). Thus, it is possible to proceed to a first check of the graphene quality. Figure 21 shows the absence of cracks or bubbles either at the border or at the center of the sample, and also the absence of remaining resist residue, indicating that we achieved a clean transfer of graphene.

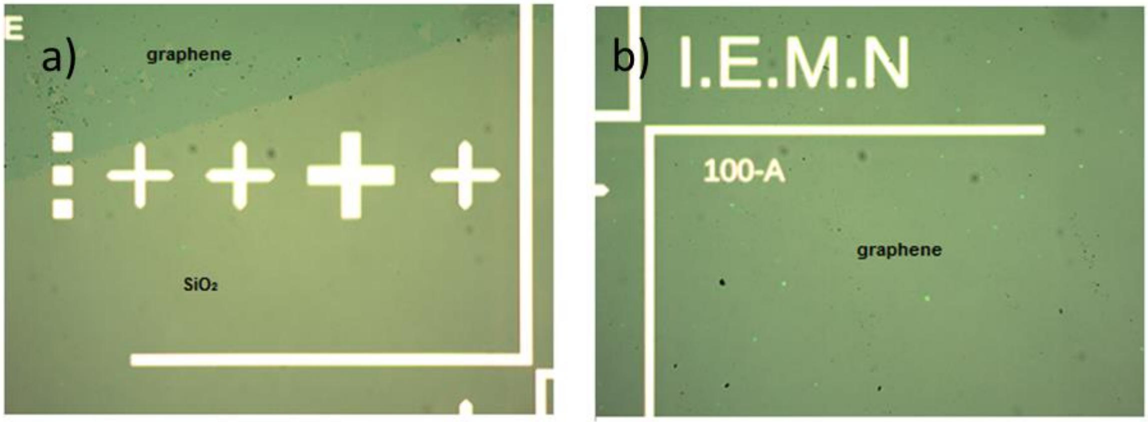

Figure 21: Optical images of graphene transferred on SiO₂ a) at the border of the sample and b) in the center of the sample

At higher magnification, using a SEM, we can also confirm the quality of the transfer as we can see in Figure 22. However, at higher magnification we can observe the presence of small wrinkles, which can lead into lowering the electronic transport of our graphene. However, the concentration of wrinkles or defects is very low. Further ameliorations on the growth can be investigated.

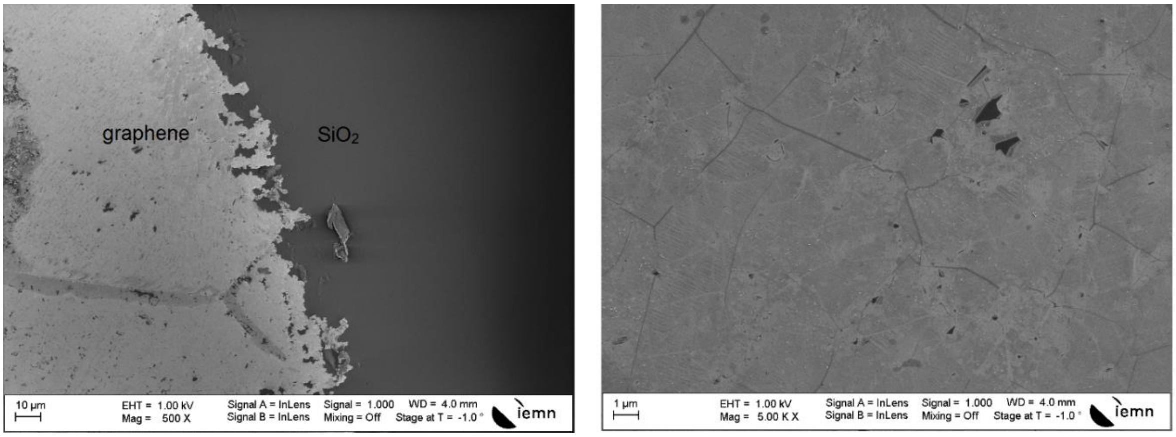

Figure 22: SEM images of graphene transferred on SiO₂

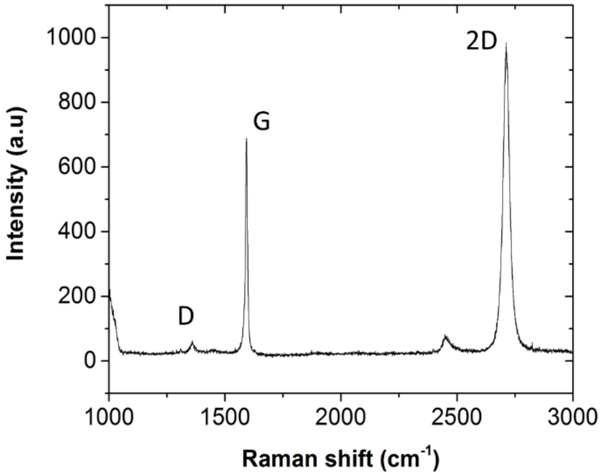

Figure 23: Raman spectra of the 3DC foam

Raman has been performed on the transferred sample as we can see in Figure 23. We can clearly identify clearly the G and 2D peaks at respectively 1590 and 2717cm^{-1} for a FWHM of 12.4 and 37.5cm^{-1}, and a weak D peak at 1360cm^{-1}, indicating a high quality graphene. The relative intensities of the G and 2D peak is around 1.5, indicating the presence of monolayer graphene. The position of the peaks did not change much compared to the spectra with graphene on copper foil. However, the relative intensities of the G and 2D peaks changed a bit, indicating residual stress in the film. This might be explained by the annealing of graphene on copper foil before the transfer because of the difference of the thermal expansion coefficient between graphene and copper. The low values of FWMH of G and 2D peaks and the absence of peak at 2900cm^{-1} indicates a clean removal of the PMMA, as compared to one can see in literature[41]. It has to be noticed that we obtained similar spectrum on all available surface of the copper foil, making the sample very homogeneous. This validates also the transfer process used in this work.

6) Growth of 2D monocrystalline graphene

Polycrystalline graphene present some lack of electron mobility because of the different orientations of the grains and the grain boundary, modifying the band structure of graphene, resulting in electron mobility lower than mobility of crystalline materials[42]. One way to bypass this problem is to use single crystals of graphene. Thus, it requires large single crystals of graphene in order to be compatible with microelectronic processes. The typical size of single crystals of graphene can be as large as millimeter size under special conditions but a lot of works present typical size around 10µm , and are usually reported with high nucleation points density (~$10^6 cm^{-2}$), limiting the size of the grains[43]. It is a challenge to reduce the nucleation density. Several approaches have been proposed, such as the use of copper oxide[44], the use of Pt as catalyst[45], or electro polishing of the copper foil[46]. We chose to treat the surface of the copper foil with a long annealing (3H) at atmospheric pressure using a strong H_2 flow (~600sccm). It appeared that we reduced the nucleation density down to $4x10^4 cm^{-2}$ as we can see in Figure 24.

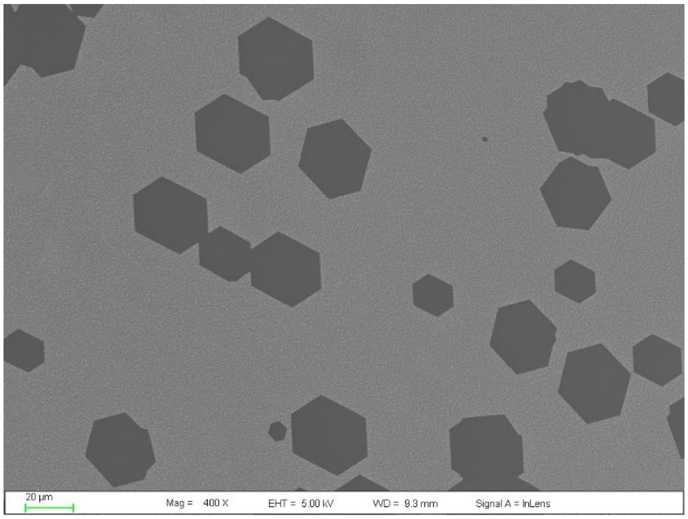

Figure 24: SEM image of single crystals graphene

With this low nucleation density, we chose to change firstly the H_2/CH_4 ratio, keeping the growth time at 2H in order to obtain large single crystals. The different parameters used in this goal are resumed in **Erreur ! Source du renvoi introuvable.** with the corresponding average size of single crystals.

H2	CH4	H2/CH4	temps	taille	
500	5.8	86.2069	2h	21	12
480	5.5	87.27273	2h	15	15
500	5.5	90.90909	2h	20	20
530	5.5	96.36364	2h	17	17
530	5.3	100	2h	20	15
530	5	106	2h	10	10
540	5	108	2h	8	8

The different sizes of the grain as a function of H_2/CH_4 ratio are presented in Figure 25. It has to be noted that the biggest grain size is around 20µm for a H_2/CH_4 ratio, corresponding to the best etching/graphene growth ratio. It is very similar to other work on the role of H_2 flow on graphene growth[47].

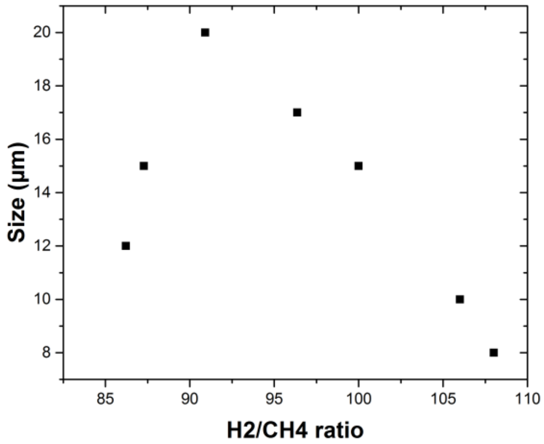

Figure 25: Average size of the grains as a function of the H_2/CH_4 ratio

Knowing the best H_2/CH_4 ratio, we chose to increase the growth time up to 5H to check the role of the growth time on the size of the grains. Different growth parameters are resumed in Table 5. It appeared that the best growth time was 4H. After 5H the size of the single crystals didn't increase, indicating that the etching and graphene growth competition achieved its saturation regime, resulting in the limitation of the size of single crystals.

H_2 flow (sccm)	CH_4 flow (sccm)	H_2/CH_4 ratio	time (H)	Size (µm)
500	5.5	90.9	2	20
500	5.5	90.9	3	22
500	5.5	90.9	4	28
500	5.5	90.9	5	27

Table 5: Growth conditions of single crystals graphene

We presented the SEM image of our best sample in Figure 26.

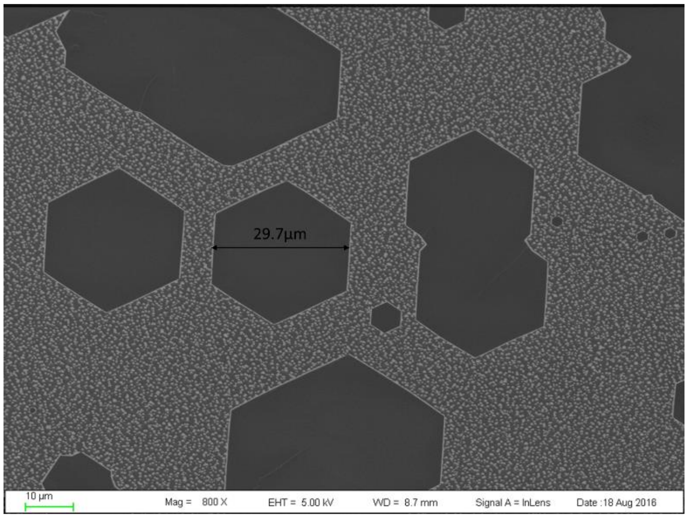

Figure 26: SEM image of single crystal graphene

We checked the Raman signal of our grown graphene. We can identify clearly the G and 2D peak at 1579.9 and 2707.9cm^{-1} respectively with a, intensity ratio of 2.3, confirming the presence of monolayer graphene. Moreover, the very weak D peak indicates a high quality graphene with very few defects.

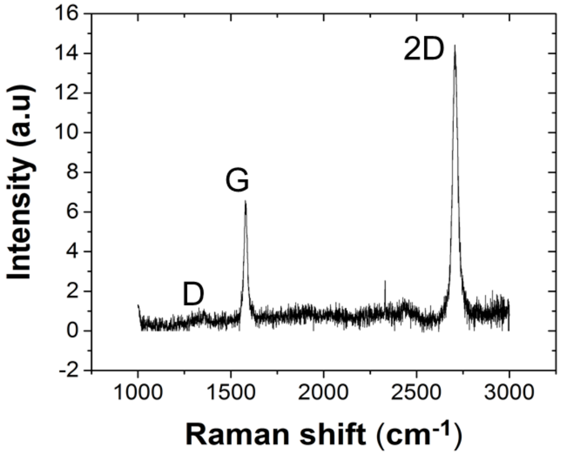

Figure 27: Raman spectra of single crystal graphene

We achieved a maximum size of ~30µm, but other studies showed bigger single crystals (up to 5mm) and lower nucleation density using other methods[44],[48],[45]. Thereby we decided to stop the investigations at this time.

III) Growth of 3D graphene

1) Growth of graphene on Nickel foam

The growth process used in this work is very similar to the growth of 2D graphene and then the growth mechanism will not be explained in detail. It consists to use a Nickel foam as a substrate which is well known for growth of multilayer graphene[49].

The substrate used for the growth of both 3DC and 3DBN is a Nickel foam from Latech[50]. It is a porous Ni foam with a purity higher than 99%, with a porosity between 90 to 98% and a pore concentration of around 100 pores per inch (PPI). An SEM image of the structure of the foam can be seen in Figure 28:

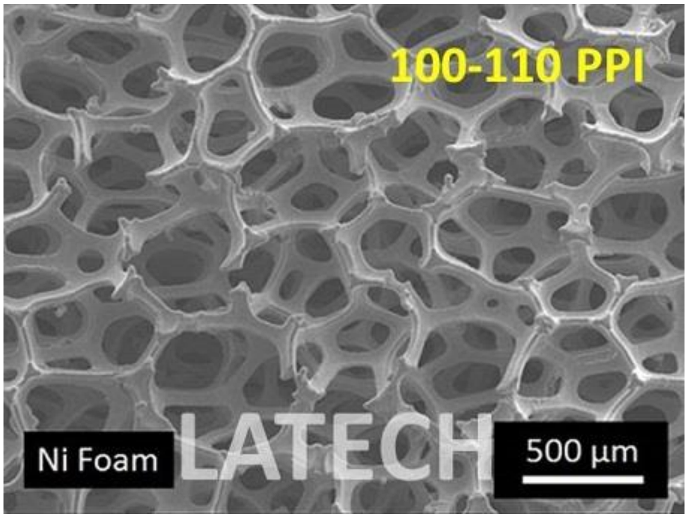

Figure 28: SEM image of the Ni foam[50]

The 3DC growth process is very similar to those of 2D graphene. It consists to expose the Nickel substrate to a mixture of dihydrogen and argon for the annealing, and a mixture of dihydrogen, argon and methane (which is the precursor) for the growth in a CVD system at atmospheric pressure[51] (APCVD). A schematic of the growth process of 3DC can be seen in Figure 29.a). The growth mechanism explained earlier allows the multilayer graphene to deposit on all available surface of the Nickel foam, adopting its porous structure.

After the growth, the foams obtained are then dip coated with PMMA, in order to protect the h-BN or the graphene and then dipped into an HCl solution for several hours (at least 15h) for the etching of the Nickel. After total etching of the Nickel, the foams are rinsed with DI water for few hours and then dried. The resulting 3D foam is then put into a slow annealing during 3h with a temperature of 700°C and a rate of 300°C/h in order to evaporate the PMMA coating (BN and graphene are stable at that temperature). This annealing allows us to prevent the use of classical dissolution of the resist in a solvent such as acetone, avoiding the resist residues issue[52]. After the annealing, we obtain pure foam of 3DC, with a similar structure and porosity to the Nickel foam used. Optical images of 3DC can be seen in Figure 29.b).

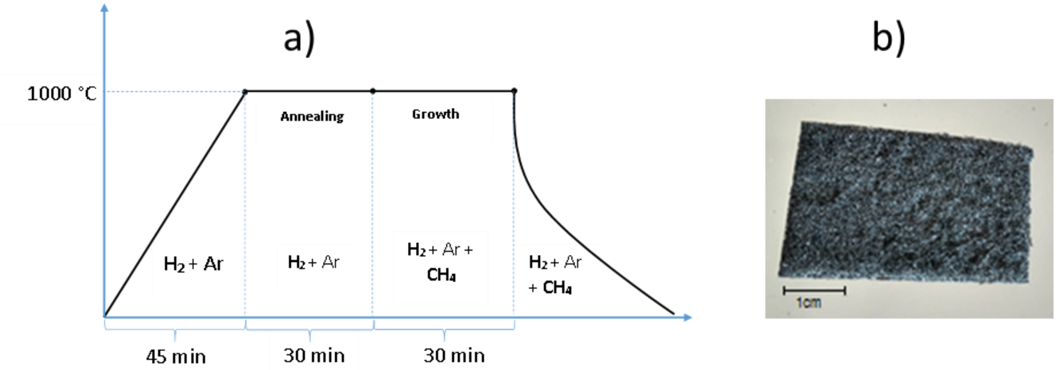

Figure 29: a) Schematic process of the growth of 3DC and b) image of a 3DC foam

2) Characterization of the Foam

In order to characterize the obtained 3DC, SEM images have been obtained and can be seen in Figure 30. Thus, we can see that the foams obtained has a similar structure and the same porosity as the Nickel foam used at first. At a higher magnification, we can see the presence of several domains, with some grain boundaries and some wrinkles. This results from the difference of the thermal expansion between graphene and the Ni foam, also observed in previous work[51].

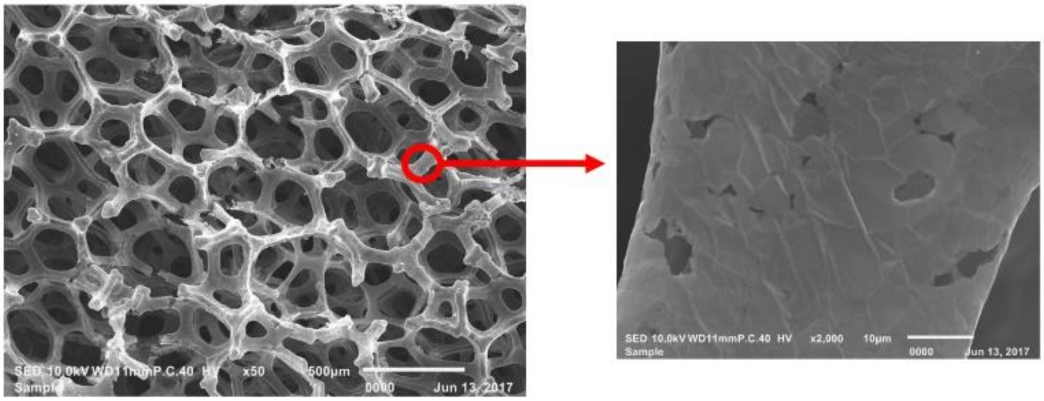

Figure 30: SEM images of the 3DC foam

Raman spectroscopy has been performed on the obtained foams and the spectrum can be seen in Figure 31. We can clearly identify the presence of the G and 2D peak located at 1582 and 2700cm^{-1} with a FWHM of 25.7 and 59.0cm^{-1} respectively. The intensity ratio of 0.72 indicates the presence of multilayer graphene. Moreover, the low intensity of the D peak on the graphene indicates the obtained graphene is of high quality according to the domain's sizes with few defects. Elsewhere, the change of intensity of the obtained peaks on few other points indicates that graphene is not homogeneous. This can be explained by the use of a Nickel foam which results in a few layers graphene[53] giving several domains with a different number of layers, with higher number of layers near the nucleation points, as we can see in Figure 31.

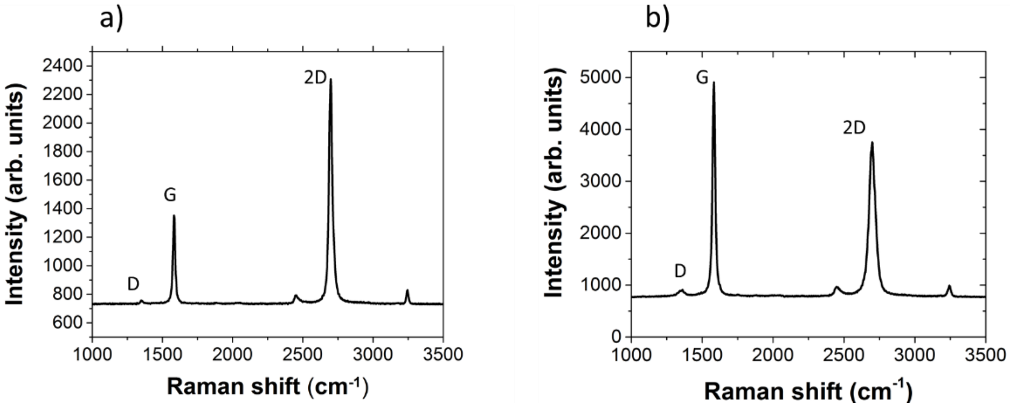

Figure 31: Raman spectrum of 3DC on two different points

IV) Growth of 2D h-BN

1) CVD growth of h-BN

Many methods have been used to synthetize h-BN of various quality. They are very similar to what have been achieved for the growth of graphene with some modifications, especially concerning the precursors. We will focus on the growth of h-BN by CVD.

Similarly, metals that can be used as catalyst for the growth of h-BN such as Ni, Cu, Co, Ru, Pt… The most commonly used precursor are ammonia borane[54] (NH_3BH_3), borazane[55] (BNH_6), borazine[56] or the combination of ammonia and diborane. All those precursors are either solid or liquid but have a common point: they are all easily evaporable by moderate heating and thus are perfect candidate for CVD process. A schematic of a h-BN growth can be found in Figure 32. As for graphene, micrometers-sized monolayers of h-BN have been grown by other work using Cu and Co substrates[57]. Indeed, the solubility of B and N are similar on those metals, in the same way as for C. However, there is some issues providing large area h-BN (wafer scale) with a good quality, either if it is multilayer or monolayer, providing a great challenge for applications in electronics. Indeed, the use of h-BN as a substrate requires large area and a very flat surface.

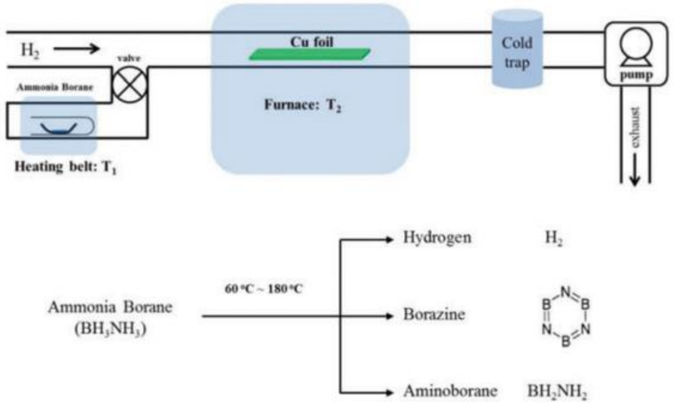

Figure 32: Schematic of the CVD of h-BN using a copper foil as a catalyst and ammonia borane as a precursor[58]

For now, only few micrometers-sized of single crystals of h-BN have been achieved in literature. We will focus on the growth of polycrystalline h-BN in order to obtain large area for applications in electronics.

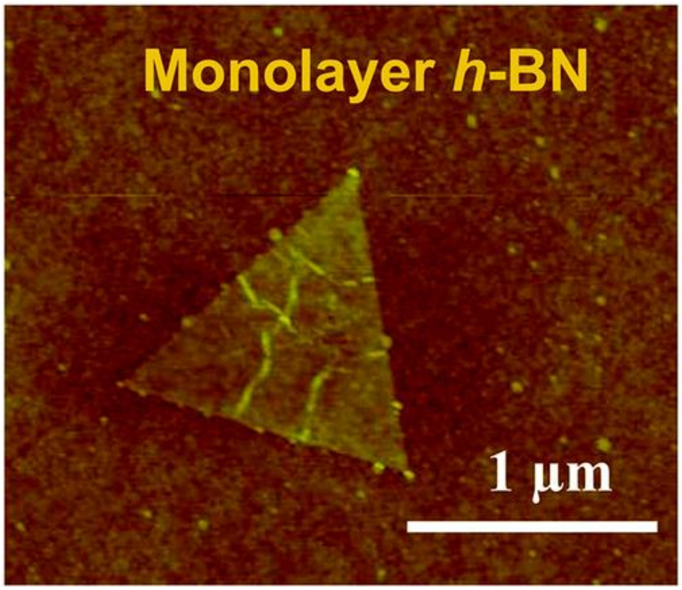

Figure 33: Atomic force microscopy image of a trigonal monolayer h-BN grain grown on Cu foil[57]

2) Growth of 2D polycrystalline h-BN

We chose to focus on the growth of polycrystalline h-BN using CVD, which is the better way to produce large area h-BN for industry. We chose to use commercial Cu foil from Alpha Aesar of high purity (99,9999%) in order to obtain monolayer h-BN, as discussed before. h-BN growth has been carried out in a Thermo Scientific Lindberg CVD, which can be seen in Figure 34. This system allows heating and cooling at moderate rates with 2 inches tube furnace. We used a mixture of 200sccm of Argon and 20sccm of Dihydrogen during all the steps. We chose a solid precursor of ammonia borane and we decided to change the amount of precursor from 6 to 11g during the growth phase. The precursor is placed at the entrance of the tube and heated at ~90°C during the growth phase.

We first cut the Cu foil in small pieces (6x2cm), clean them with acetic acid, acetone and IPA under ultrasound in order to remove all possible copper oxide and to have the cleanest surface possible. We then put the pieces in the middle of the tube furnace. We proceed to a high vacuum ($<5.10^{-5}$ bar) before starting and then we start the heating for 40min from room temperature to 1000-1050°C, then the annealing for 1H, we continue with the growth for 30min and we finish with a moderate cooling by stopping the heater and let the temperature of the tube decrease down to room temperature. A schematic of the growth process can be found in Figure 35.

Figure 34: Image of the tubular CVD used in this work

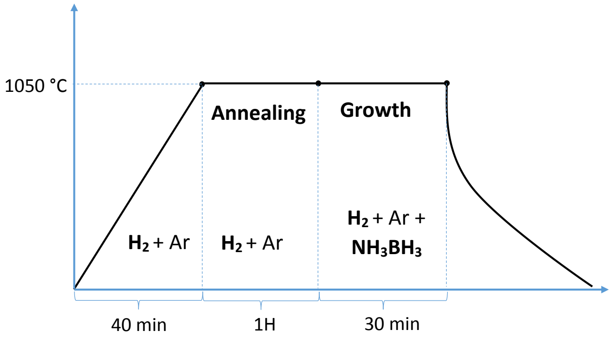

Figure 35: Schematic of the growth process of h-BN

3) Characterization of the grown h-BN

For all the different growth made, we performed optical images, SEM images, and Raman spectroscopy. The optical images and the SEM images of our samples tends to show that we have full covered h-BN. We first tried to vary the quantity of precursor from 6 to 11g to achieve good growth conditions. For the growth with a low quantity of precursor (6-8g of ammonia borane) no Raman spectra have been obtained, indicating bad quality of the h-BN. From 9 to 11g of ammonia borane, a weak Raman signal has been obtained at ~1370cm^{-1} as observed in literature[59],[60], indicating the presence of h-BN. However, for samples with high quantity of precursor we observed the presence of multilayer at the nucleation point, as we can see in the following SEM image:

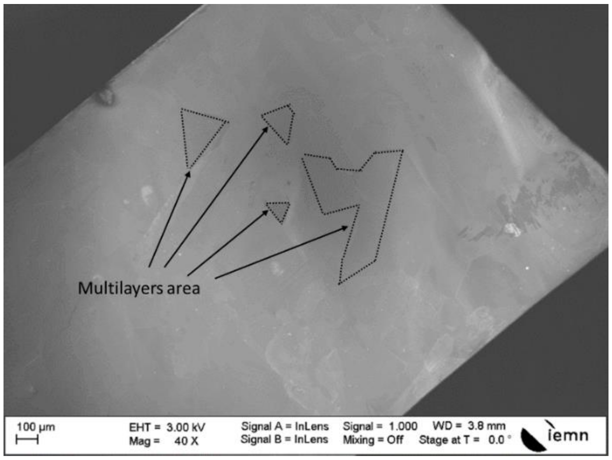

Figure 36: SEM image of h-BN on copper foil with the presence of multilayer regions

All these growths have been carried out with a growth temperature of 1050°C.

Table 6 shows the different observations made with the help of Raman spectroscopy and SEM images. The best quantity of precursor seems to be 9g of ammonia borane.

Quantity of Ammonia borane (g)	Raman signal	SEM observations
6	No signal	Seems full covered

7	No signal	Seems full covered
8	Weak signal	Seems full covered
9	**Good signal**	**Seems full covered**
10	Good signal	Seems full covered with the presence of multilayer regions
11	Good signal	Seems full covered with the presence of multilayer regions

Table 6: Observations of the characterized samples made with Raman spectroscopy and SEM with different quantity of precursor

We chose to present the best sample that we grew, according to the characterization performed, using 9g of ammonia borane**.**

The samples have been cut into 3 pieces of ~2cmX2cm. Two pieces have then been transferred and characterized. We will focus now on these two pieces, named sample 1 and sample 2 in the following description. We can see that the two samples are very similar and have the same size. We can also see at optical microscope that the copper is homogenous, with similar copper grain size.

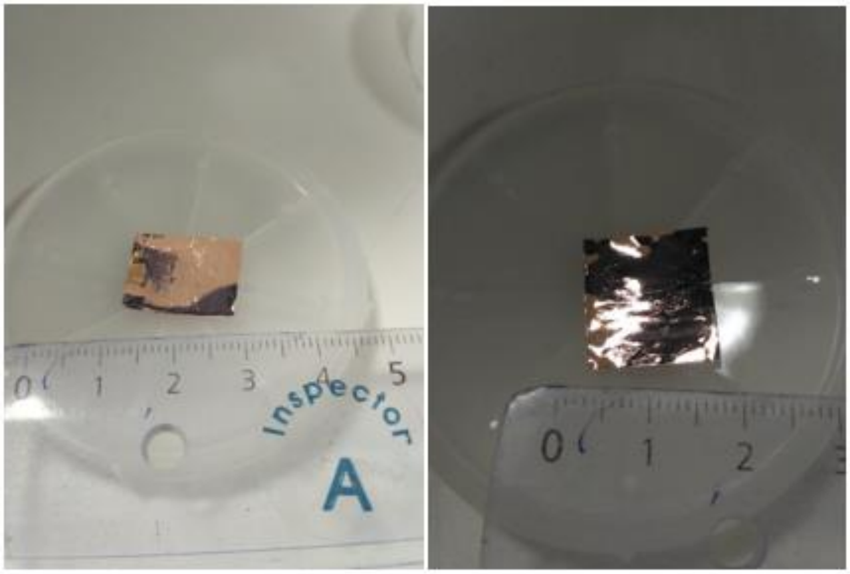

Figure 37: Optical images of sample 1 and sample 2

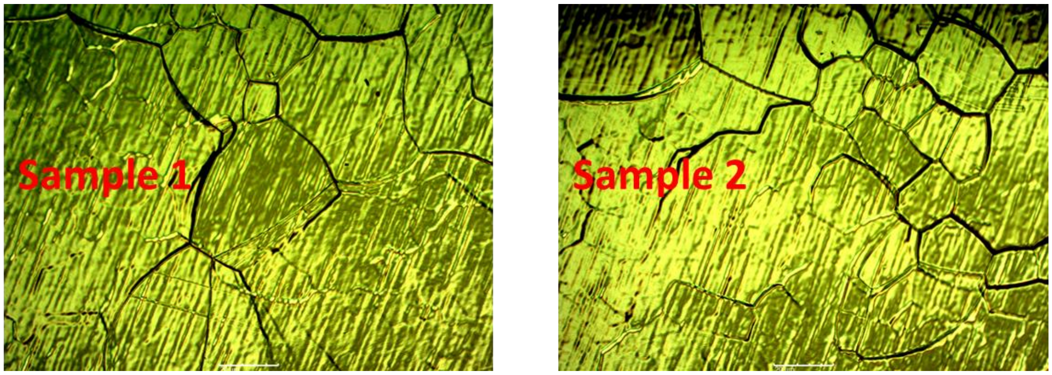

Figure 38: Optical images of h-BN on copper

The SEM images at low and higher magnification are also indicating that we have a full covered sample, confirming the growth conditions, with similar structure of grains and grains boundaries.

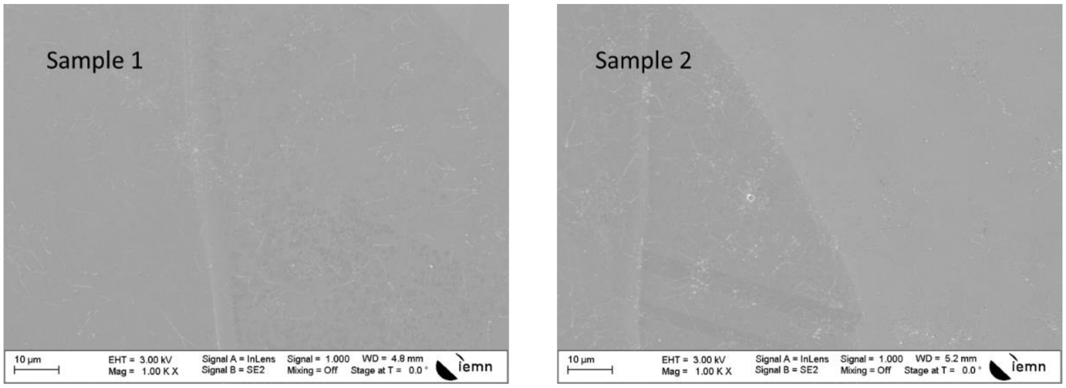

Figure 39: SEM images of h-BN on copper

Raman spectroscopy has been performed on our samples. We chose different areas to compare the Raman signal on all surfaces. For both samples we found similar Raman spectrum with the typical peak of h-BN located at 1370cm^{-1} originating from the boron-nitrogen bond stretching. Although the signal is pretty weak, it is comparable with other publications on monolayer h-BN[59],[60]. The FWMH of the peak is always around 5-7cm^{-1}. The position of the peak and the FWMH seem confirming the presence of a monolayer of h-BN[61]. Moreover, we obtained similar spectrum on all available surface, confirming the good conditions of the growth to obtain a full covered film of h-BN

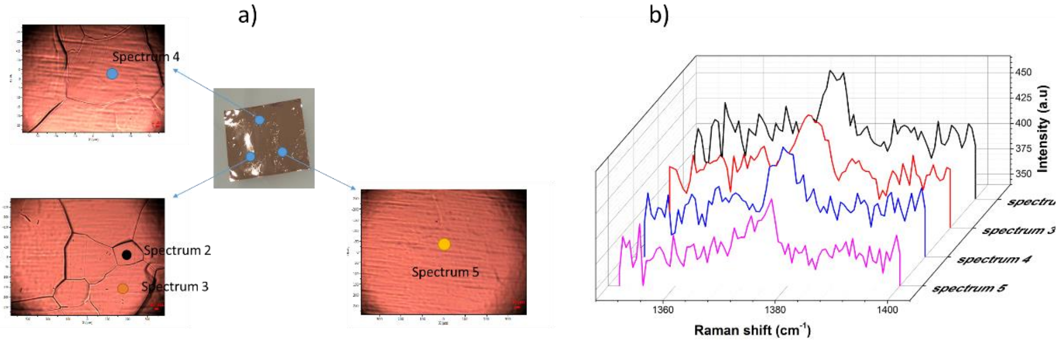

Figure 40: Different Raman spectrum performed on h-BN on copper. Sample 1

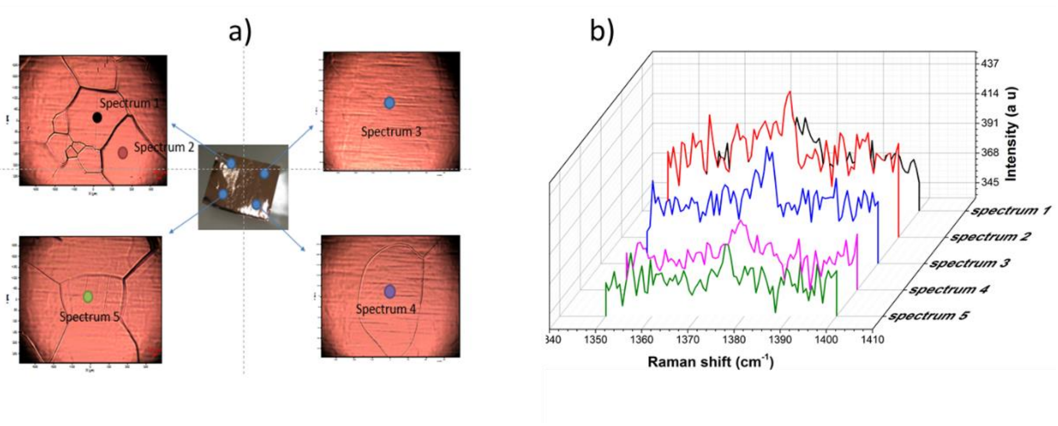

Figure 41: Different Raman spectrum performed on h-BN on copper. Sample 2

XPS spectroscopy was carried out on our sample with the Help of Dominique Vignaud and Jawad Hadid in order to determinate the elemental composition and the stoichiometry of our h-BN. We attributed the 397.6 and 190.1eV peaks to N1s and B1s respectively, as expected for h-BN[59], confirming the presence of a pure h-BN sample.

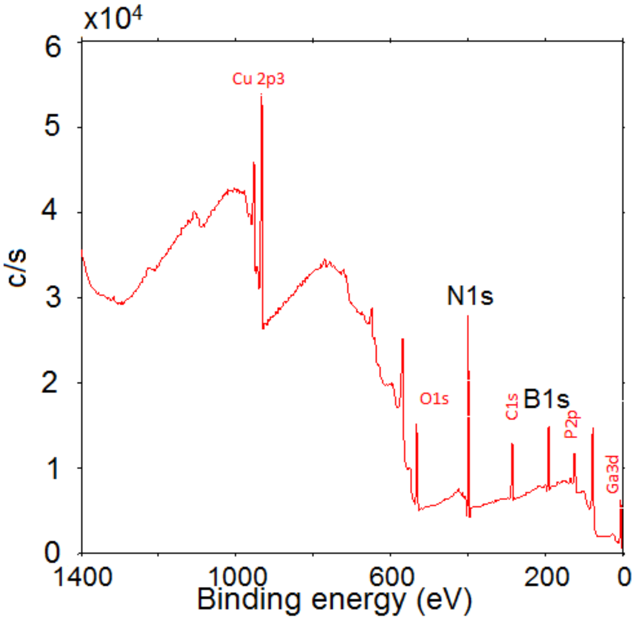

Figure 42: XPS spectra of h-BN on copper

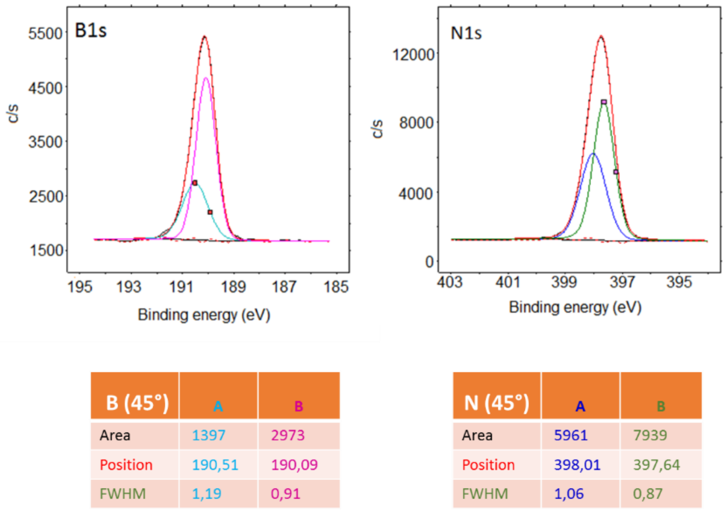

B (45°)	A	B
Area	1397	2973
Position	190,51	190,09
FWHM	1,19	0,91

N (45°)	A	B
Area	5961	7939
Position	398,01	397,64
FWHM	1,06	0,87

Figure 43: Peak parameters from the XPS signal

4) Transfer and characterization of h-BN

A good and clean transfer of h-BN is essential for potential applications in electronics. Thus, we tried to use what have been achieved with the graphene transfer and to adapt it to the transfer of our samples of h-BN. We will present a second method of transfer called bubbling transfer which has been optimized by another PhD student (Soukaina BEN SALK from CARBON group) on graphene. We will present the characterization performed on the two best samples presented earlier.

a) Method of transfer

Two methods of transfer have been used: the wet transfer and the bubbling transfer. **First,** we adapted the wet transfer of graphene with h-BN. Several improvements have been made. Due to the difference of surface tension between graphene and h-BN, we modified the deposition parameters of PMMA to achieve a protection layer of the same thickness. As h-BN is less chemically active than graphene, an O_2 plasma etching of the back face is not suitable (chemical etching). We preferred to use an Ar etching (physical etching).

We checked with Raman spectroscopy that the back side was fully etched from h-BN. The other steps of the wet transfer remain the same as for graphene and can be found in Figure 19. An optical image of sample 1 before and after wet transfer can be found in Figure 44.

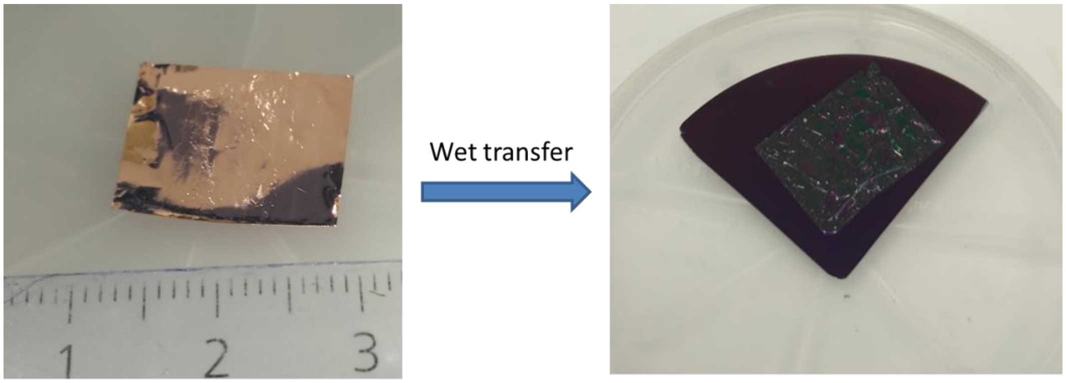

h-BN on Copper

h-BN with PMMA on SiO_2/Si

Figure 44: Image of h-BN before and after transfer

The second method used for the transfer of h-BN is the bubbling transfer. Its steps are similar to the wet transfer. Its main difference is the separation of the PMMA/h-BN with the copper. Instead of etching the copper we separate the h-BN from the copper based on an electrolytic solution. Its principle consists to apply a continuous voltage between the cathode formed by the copper foil covered with h-BN, and the anode formed by a graphite stem (purity of 99.997%) in an electrolytic solution made with potassium hydroxide KOH of 0.1mol/L concentration. A voltage of 2.6V is applied between the two electrodes, generating the formation of H_2 bubbles at the h-BN/Cu interface following the equation:

$$2H_2O\ (l) \rightarrow\ H_2\ (g) + 2OH^-\ (aq)$$

A schematic of the bubbling transfer process can be found in Figure 45.

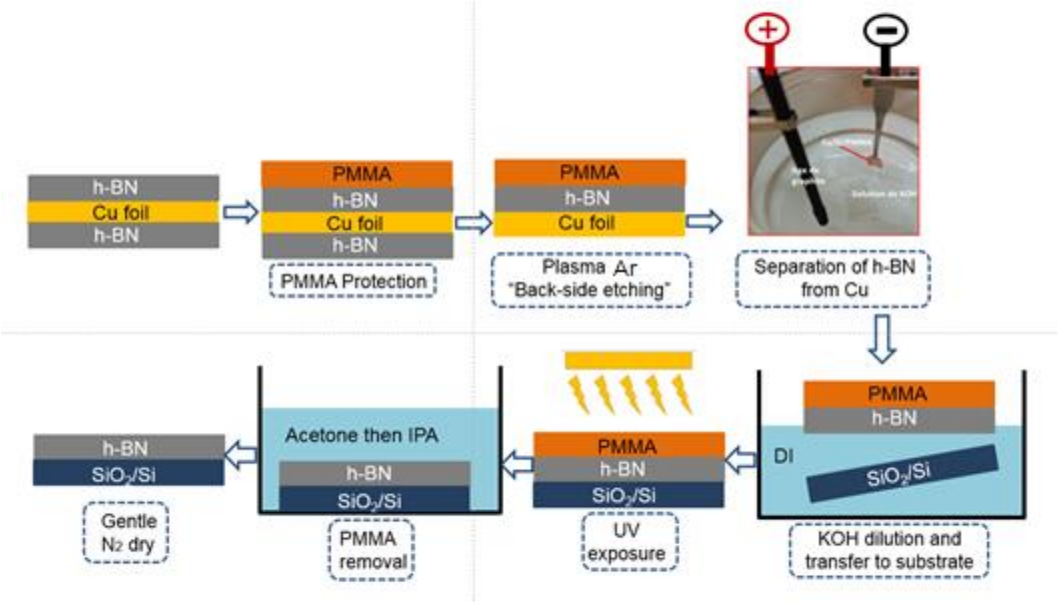

Figure 45: Schematic of the bubbling transfer process

The following steps of the process remains the same as for the wet transfer. The advantage of the bubbling transfer is its rapidity of utilization. Indeed the etching of the copper for the wet transfer requires several hours for the copper to be completely etched. The bubbling transfer allows a separation of h-BN in only few minutes.

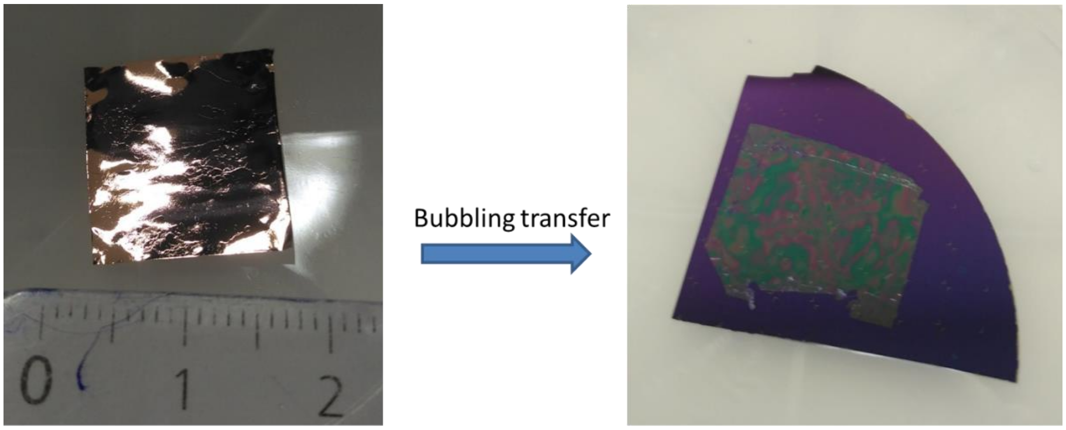

h-BN on Copper

h-BN with PMMA on SiO$_2$/Si

Figure 46: image of h-BN before and after bubbling transfer

b) Characterization

Optical microscopy has been carried out on our two samples and the images show a good and clean transfer of h-BN onto SiO_2, confirming both methods of transfer.

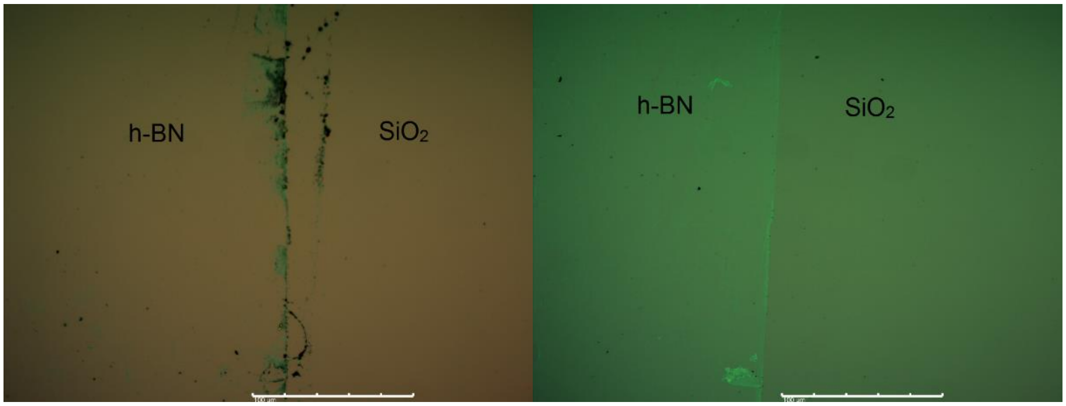

Figure 47: Optical images of h-BN (sample 1 and sample 2) transferred on SiO_2

SEM images show that after transfer, both samples present h-BN on all available surface. Images show a similar aspect of the h-BN surface concerning the grain size and grain boundary of h-BN.

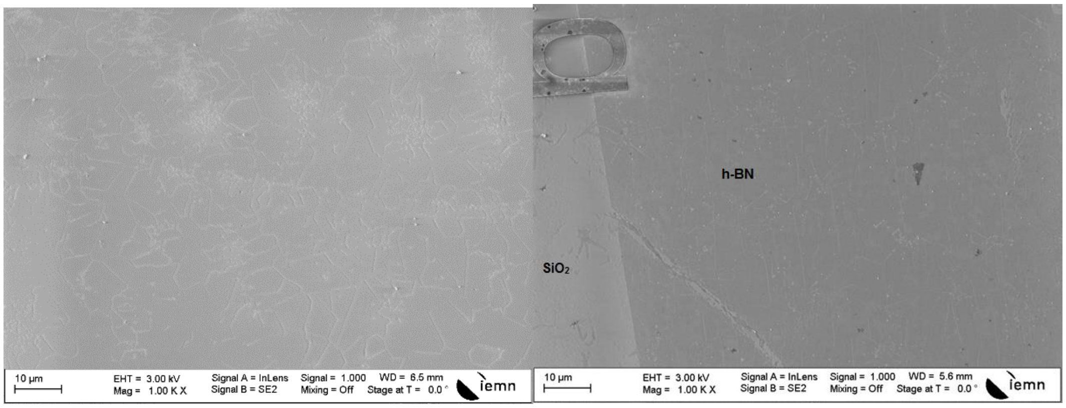

Figure 48: SEM images of h-BN (sample 1 and sample 2) on SiO_2

Raman spectroscopy has been carried out on the two samples. We detected a weak peak located at 1370cm^{-1} similar to one can find in literature[59],[60], confirming the presence of h-BN on all surface. We can note that the FWHM increased after transfer by 3 to 4 times (4.5cm^{-1} to 16cm^{-1} average), which can be explained by the increased strain and stronger surface scattering in h-BN[62]. This validates both methods of transfer.

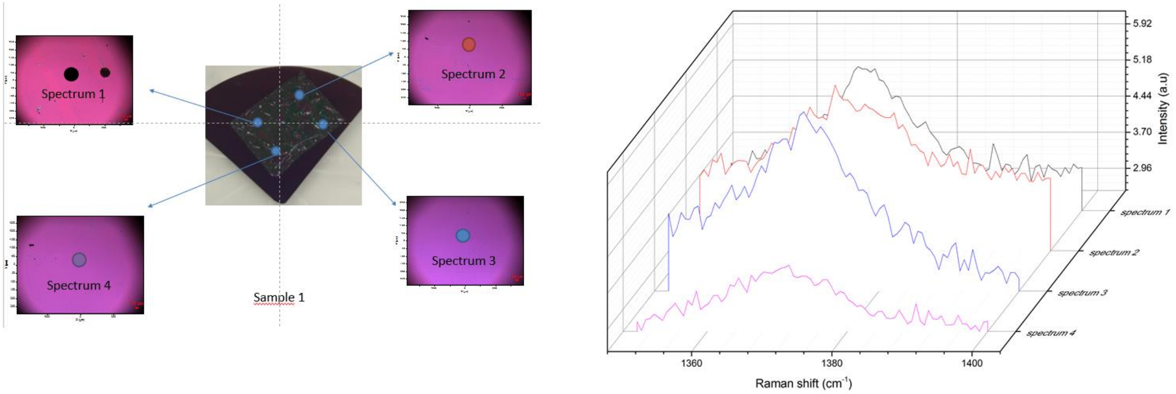

Figure 49: Raman spectrum of sample 1

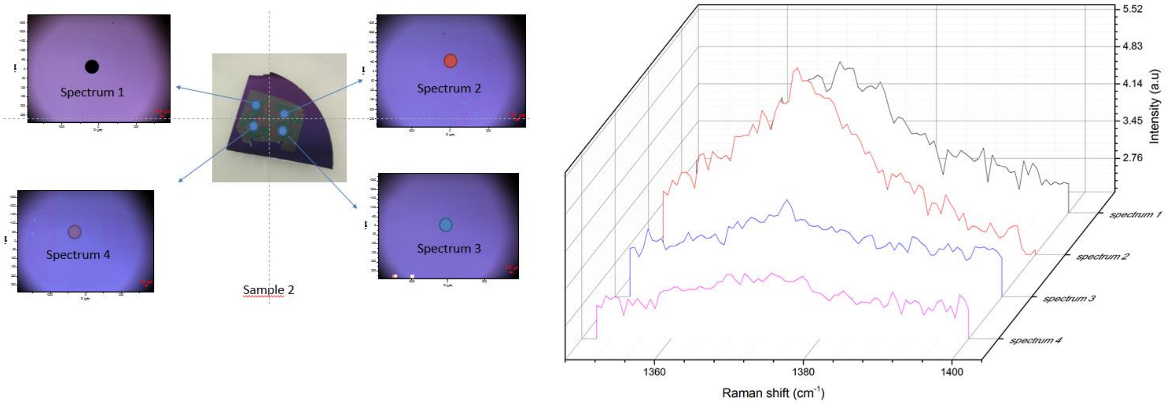

Figure 50: Raman spectrum of sample 2

V) Growth of 3D h-BN

1) Growth of h-BN on Nickel foam

The 3DBN growth consists as a similar growth process, with the same gases for the annealing. The precursor used for the growth of 3DBN, as for the growth of h-BN is ammonia borane (NH_3BH_3), which is a solid precursor[54]. The precursor is placed at one side of the tube, where the gas comes in, and is then evaporated at a temperature between 80 to 100°C. In contrary with the 3DC growth, the use of low pressure (LPCVD) is required in order to avoid too thick films of BN and the presence of sp^3 like NH_3-BH_3[63]. In the same way as graphene, multilayer h-BN is deposited on all available surface of the Ni foam, adopting its mechanical structure.

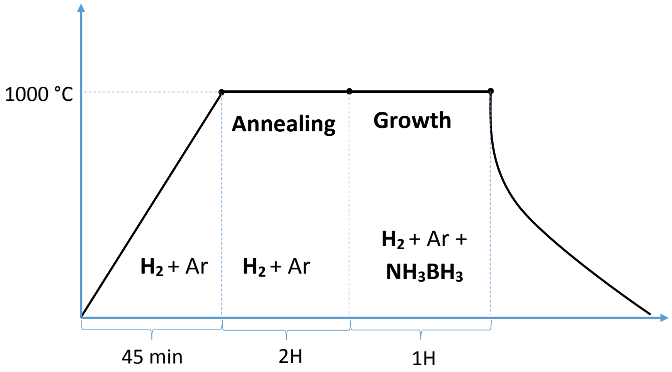

Figure 51: Schematic of the 3DBN growth process

2) Characterization of the foam

Optical image can be found in Figure 52.a) showing a similar structure and porosity as the Ni foam.

Raman spectroscopy has been performed on the obtained foams and the spectra can been in Figure 52.b). We can clearly identify the presence of the E_{2g} peak for the BN at 1377cm^{-1} with a FWHM of 44.6cm^{-1}, indicating the presence of multilayer h-BN. Elsewhere, the change of intensity of the obtained peaks on few other points indicates that h-BN is not totally homogeneous. This can be explained by the use of a Nickel foam which results in a few layers h-BN, giving several domains with a different number of layers.

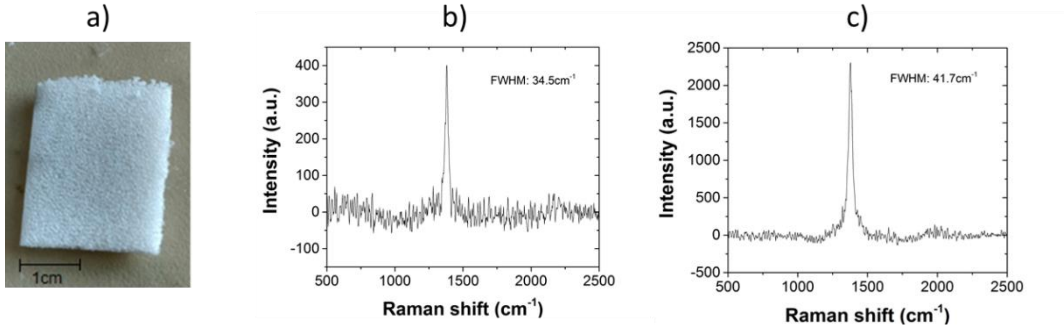

Figure 52: a) image of a 3DBN foam. b) and c) Raman spectrum of the 3DBN foam on two different points

VI) Conclusion

In this chapter, we confirmed the growth conditions of polycrystalline graphene with a full cover of the copper foil used as a catalyst and we validated the clean transfer of graphene using the optimized wet transfer method. We showed the optimization process of the growth of single crystals of graphene by varying the H_2/CH_4 ratio and the growth time. We achieved a size of 30µm, which is bigger than comparative work, but too small compared to other techniques presented in other work (up to 5mm). We obtained the good growth parameters for the growth of full covered polycrystalline h-BN and we validated the transfer of h-BN using wet transfer and bubbling transfer. We presented the process to obtain thick materials composed of 2D materials using the growth of graphene and h-BN on a nickel foam, resulting in 3DC and 3DBN foam, with the same structure and porosity as the substrate.

Chapter 2: 3DC and 3DBN foam infused with polyimide

I) Introduction

Since 1960, both industry and researchers gained interest into flexible electronics due to their unique properties such as being lightweight, bendable, conformable, rugged and good mechanical strength. A big interest is also growing for such substrates because of their availability to be compatible with roll to roll processes, which can lead to easier processes, which has also an impact on economy of electronic processes. Those properties raise interest in many applications such as photovoltaics[64], organic light emitting diodes[65], displays[65], lighting[66], radiofrequency identification systems (RFID)[4], image and chemical sensors[67]. All those technologies are developed with a great variety of materials from polymers to thin film inorganic semiconductors or hybrid materials.

In electronic, three flexible materials are largely used: polyethylene terephthalate (PET), polyethylene naphthalate (PEN) and polyimide (PI). PEN and PET are the two main transparent flexible substrates used in flexible electronics but have a poor tolerance to temperature. PI is non transparent but present a high transition glass temperature (T_g~360°C)[68] which allows it to be used for electronics which use a great range of temperature. However PI presents a low thermal conductivity[69], which limits its use for high power electronics. Indeed the thermal conductivity of PI is in the range of $0.24W.m^{-1}.K^{-1}$ [70] which is quite low compared to crystalline Si which has a thermal conductivity around $100W.m^{-1}.K^{-1}$ [71]. Such a difference results in a reduction of power of devices on PI, in order to decrease the local heat generated.

One way to mitigate this issue is to infuse higher thermal conductivity materials into the polymer matrix to improve its overall conductivity. Recently, there is a growing interest to use highly thermally conductive nanomaterials as nanofillers for infusing into the matrix. Nanomaterials such as graphene[72], carbon nanotubes[73] and metallic nanoparticles[74] are common fillers for these purposes. Although improvements of the overall conductivity can be obtained using this approach, there are still drawbacks, such as agglomeration of the filler and high filling fractions[75].

In order to bypass this issue and obtain a high thermal conductivity material for electronics, we developed a new composite material to increase the heat spreading across the material. The idea is to fill the PI with a 3D foam material, which is composed by an interconnected networked structures with multilayers of graphene or h-BN, which are well known for their high thermal conductivity[10],[53].

To obtain such a material, we developed the growth of 3D foam using a CVD process, and we infused this 3D foam with some PI. A flat thin flexible substrate is obtained, and their physical properties have been investigated in order to validate its use in high power flexible electronics.

II) Infusion of 3D foam with polyimide

1) First generation of substrate

The infiltration process consists of a multiple step process, involving the use of poly(amic acid) (PAA) diluted in N-Méthyl-2-pyrrolidone (NMP), which chemical structure can be seen in

Figure 53.

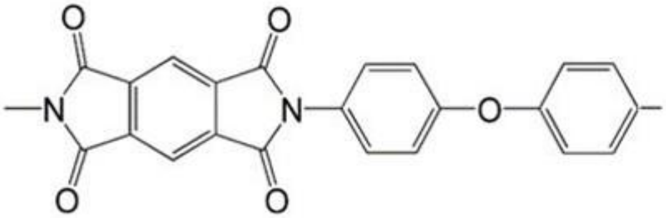

Figure 53: Chemical structure of poly(amic acid)

Residual stress is a major problem of infiltration mechanism, mainly due to the evaporation of the solvent[76] (in our case NMP). We decided to decompose the infusion of the foam into several steps, using diluted poly(amic acid), starting from a highly diluted solution to a more concentrated solution. This allows a better penetration of the solution and avoids the formation of strain in the film. The schematic of the multiple steps infusion can be seen in Figure 54.

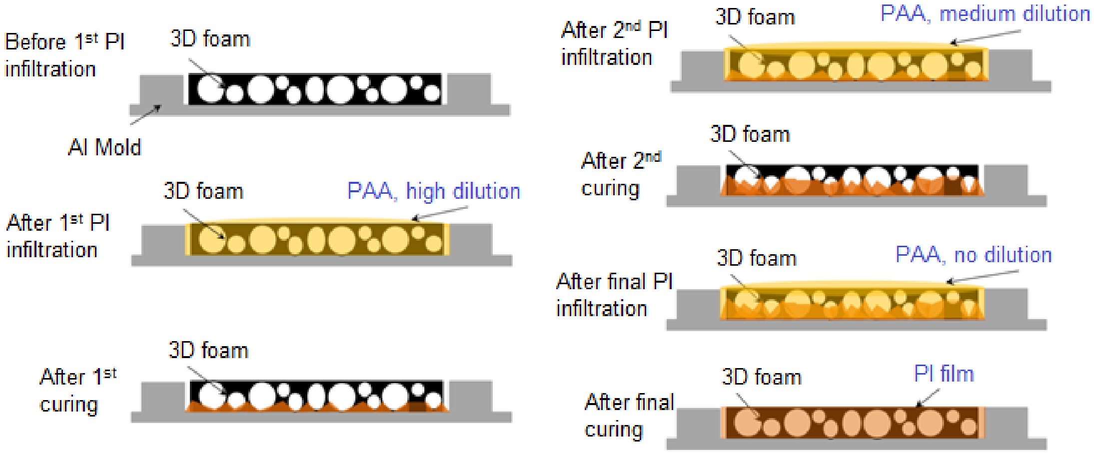

Figure 54: Schematic of the 1st generation film preparation process

It starts with a highly diluted solution poured onto the foam, then a curing at 350°C for 1h30min under N_2 flow, enabling the imidization of the poly(amic acid). A thin film of PI is obtained at the bottom of the foam. We then poured again a less diluted solution and cure again. We repeat this step until the PI infiltrated all the foam in its thickness. For the first generation of substrates we used an aluminum mold to pour the poly(amic acid), but this techniques resulted with films with a high roughness on both faces, making our material non compatible with microelectronics. An optical image of the obtained films can be found in Figure 55

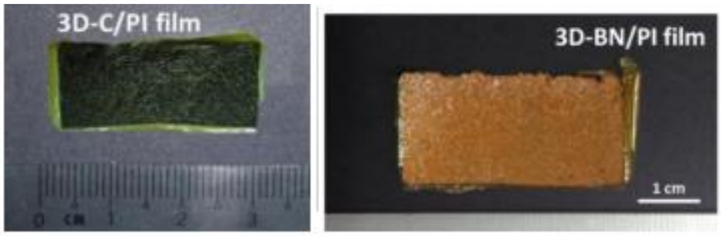

Figure 55: Optical images of 3DC/PI and 3DBN/PI substrates

2) Second generation of substrate

In order to obtain a very flat surface on one side of the film obtained, the second technique used consists of the use of a Si wafer as the bottom limit. The process remains the same, consisting of using a highly diluted solution of poly(amic acid) at first, then cure the material and repeat with solutions more concentrated until the foam is completely filled with PI. When the last curing is performed, we just need to peel off the obtained film from the Si wafer. This peeling is possible due to the reduced surface adhesion between the film and the oxide layer on the Si wafer[77]. We will show that by that way we obtain films with a much higher smoothness.

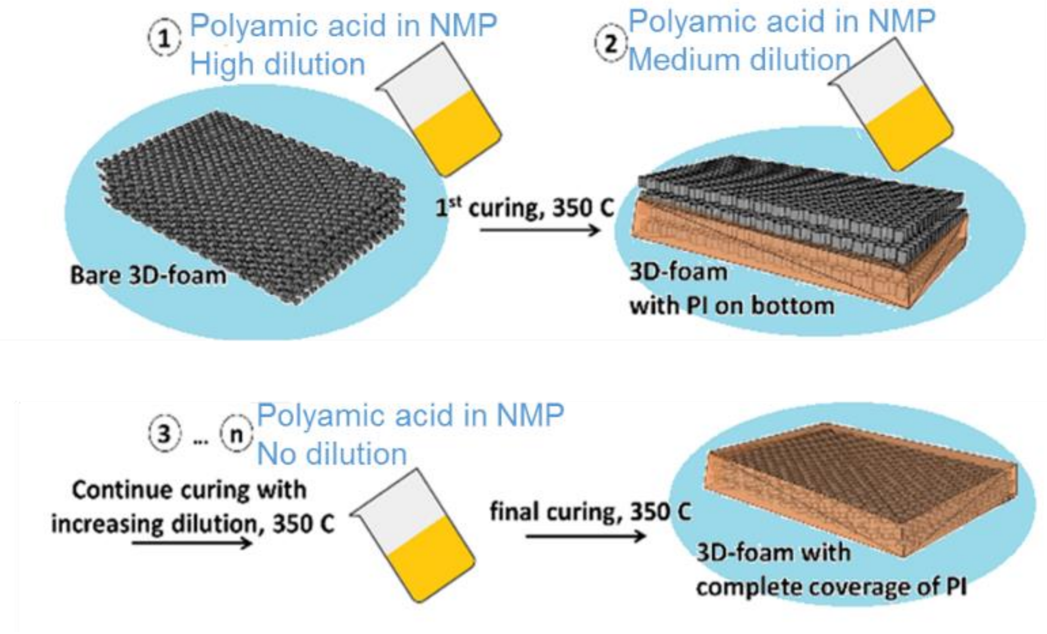

Figure 56: Schematic of the second generation film process

III) Characterization of the substrates

1) Mechanical properties

The smoothness of the surface of the samples of the first generation (using a mold) has been checked by 3D imaging using an optical microscope. We found a roughness of 16.25µm and at some local points some gap of around 50µm, making our samples incompatible with standard microelectronics processes such as e-beam lithography. This comes from the production process and we decided to no longer use a mold but to use a Silicon wafer as the bottom limit, making one of the surfaces very flat.

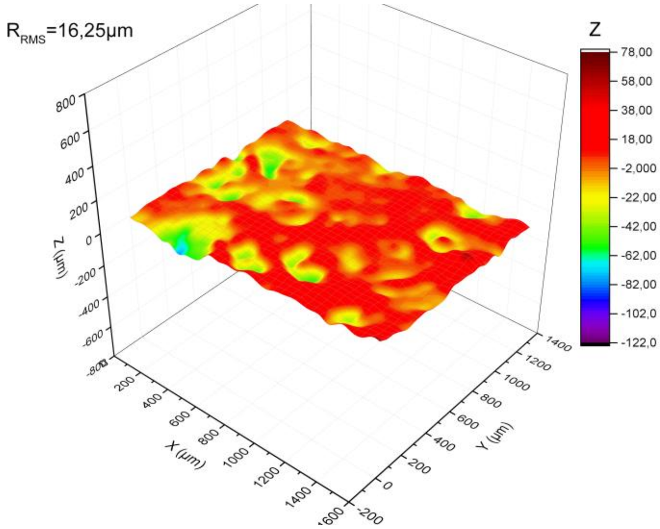

Figure 57: 3D mapping of the substrates of first generation

Samples from 2nd generation were too smooth to obtain 3D images with the optical microscope. We used a profilometer Bruker DektaXT to obtain the roughness of the top surface of our samples and we compared it with a commercial Kapton, as we can see in Figure 58. We found a roughness of 516.6nm for the samples of 2nd generation and 71.5nm for a commercial Kapton, which put the light on the improvements of the surface made by the 2nd generation process. This allows us to use such a substrate for microelectronic process.

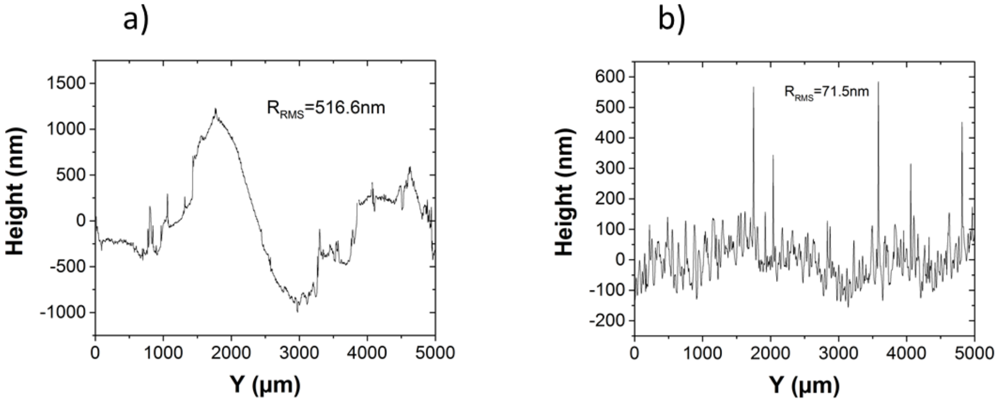

Figure 58: profilometry measurements of a) Samples of 2nd generation and b) commercial Kapton

AFM images have been performed on PI infused 3DC of second generation in order to check the smoothness of the surface and its compatibility with most microelectronics process. We obtain a local RMS roughness of 10.86nm, which is way better than the first generation samples and allows us to use this film for microelectronic processes. A similar roughness has been obtained on several areas of the samples, making it very homogeneous.

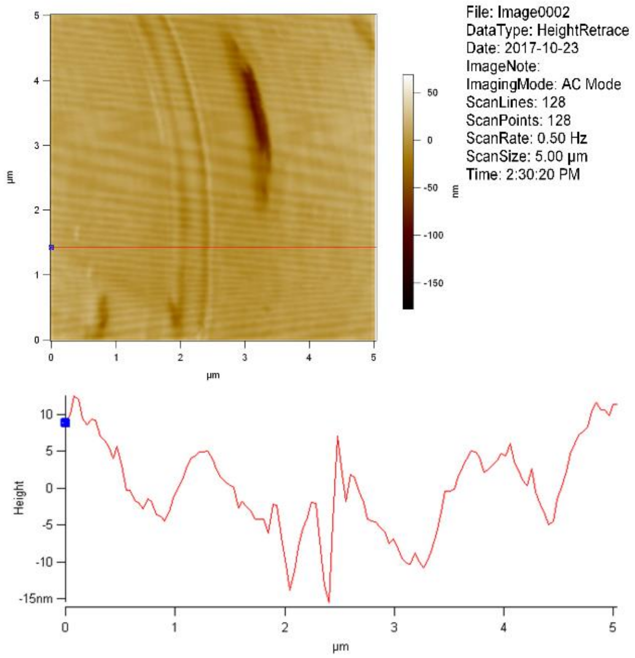

Figure 59: AFM images of the substrates of second generation

Graphene and h-BN are often used for flexible electronics[78],[79],[80] due to their mechanical properties. The film we obtain presented a good flexibility, as it can be seen in Figure 60. Indeed, the insertion of 3DC or 3DBN seem not to affect the flexibility of the PI. Also, a series of flexion and deflection has been applied to the material and no deformation has been observed on the sample.

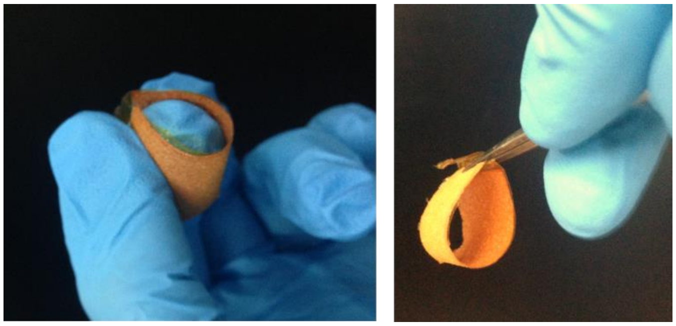

Figure 60: Optical images showing the good flexibility of our samples

In order to study the mechanical properties of our films, tensile tests have been performed using an INSTRON 5567. The setup can be found in Figure 61:

Figure 61: Set up of the stretching test using INSTRON 5567

Samples have been cut into the same design and then compared with a commercial Kapton. Stress-strain curves of commercial Kapton and PI infused 3DC can been seen on Figure 62. We obtained a Young Modulus of 2.64GPa for the commercial Kapton and 1.72Gpa for the PI infused 3DC, which is in the same order of magnitude. The difference can be explained by the different techniques used to obtain Kapton and our samples. Moreover, we obtained a tensile strain at rupture of 10% for the PI infused 3DC against 5% for the commercial Kapton. This can be explained by the high tensile resistance of the graphene, which allows a higher deformation before rupture of our films.

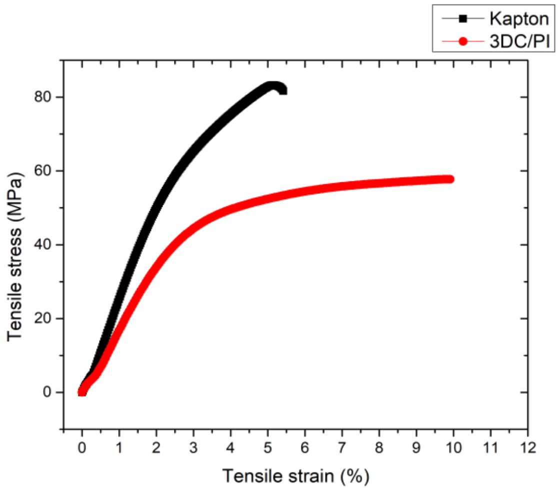

Figure 62: Stress-strain curves of commercial Kapton and PI infused 3DC foam

2) Electrical properties

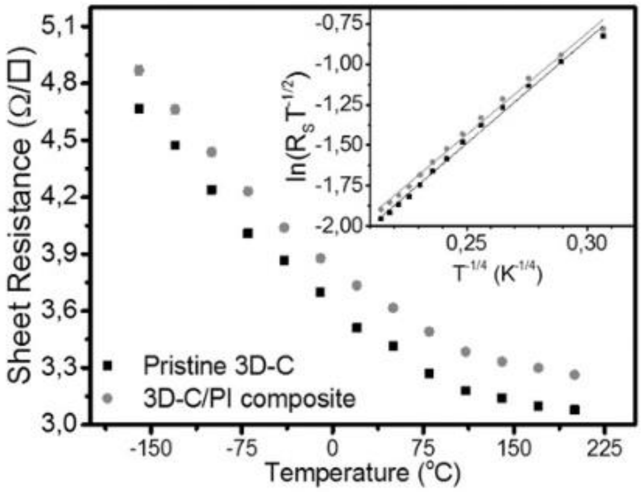

Figure 63: Sheet resistance of bare 3D-C and 3D-C/PI at a temperature range of −160 to 200 °C (inset: fit of VRH model, that is ln(RT$^{-1/2}$) versus T$^{-1/4}$ for both materials)

Figure 63 shows the results of sheet resistance measurements performed on bare 3D-C (black squares) and 3D-C/PI composite film (red circles) at a temperature range from −160 to +200 °C. Both curves show the same behavior, with the maximum electrical sheet resistance of about 4.8 Ω.sq^{-1} at −160 °C, which decreases proportionally with rising temperature and reaches the minimum of about 3 Ω.sq^{-1} at +200 °C. These results indicate that the PI infiltration into 3DC does not cause any parasitic effect on its intrinsic electrical conductivity. The average sheet resistance measured for ten different 3DC/PI samples of the same thickness (218 ± 22 μm) at room temperature was found to be 4.9 ± 1.16 Ω.sq^{-1}.

In order to have a better understanding of the electrical conductivity behavior, the results have been fitted with several conduction behaviors. Both samples have been found to fit very well the variable range hopping (VRH) model by Godet[81] as shown in the inset of Figure 63. The sheet resistance Rs (Ω.sq^{-1}) follows a VRH behavior due to carriers hopping between energy levels within band-tails, described by:

$$R_S(T) = R_{00}T^{1/2}\exp\left(\left(\frac{T_0}{T}\right)^{\frac{1}{1+d}}\right)$$

Where R_{00} is the band tail's resistivity prefactor, T_0 (K) is the temperature coefficient that contains the hopping parameters, i.e., the density of states and the localization length of the wave function and d is the hopping space dimensionality. The results fit the VRH model with a $T^{-1/4}$ temperature dependence, d = 3. This indicates a 3D electronic conductivity in both the bare 3DC and 3DC/PI samples. The 3D VRH electronic transport mechanism suggests that the electrical conductivity in the 3DC skeleton involves carriers hopping between energy levels within band tails located at the graphene sheets grain boundaries. Similar electrical conduction behavior have been reported by both Godet[81] and Li et al.[82] for CNT bundles, CNT fibers, and other carbon based materials.

The temperature dependence of the films sheet resistivity was compared with other carbon materials according to the VRH model. The prefactor σ_0^* and slope $T_0^{1/4}$ were extracted according to the equation:

$$\sigma(T) = \sigma_0^* T^{-\frac{1}{2}} exp\left(-\left(\frac{T_0}{T}\right)^{\frac{1}{4}}\right)$$

Which is the conductivity equivalent description of the previous equation, where σ is related to the conductivity (S.cm^{-1}) of the samples. The extracted values of the 3D-C/PI film are similar to those of the bare 3D-C sheet, suggesting that the original conductivity mechanism of the 3DC was preserved after the PI infiltration. In addition, the value of the localization parameter $N(E_F)\gamma^{-3}$ was calculated according to the equation:

$$N\ (E_F)\gamma^{-3}T_0 = 310$$

where $N(E_F)$ is the density of states near the Fermi level, $1/\gamma$ is the decay length of the electronic wave function, and $T_0^{1/4}$ is the slope extracted from previous equations. The values calculated for the localization parameter in the case of 3DC and 3DC/PI are respectively 126 and 76 eV^{-1}. These large values of localization parameter ($N(E_F)\gamma^{-3} >> 10^{-5}$) indicate a very weak electronic localization. This is expected for a material composed of graphene layers, in which the electrical conductivity is weakly affected by phonon scattering.

3) Thermal properties

Thermal properties are the main goal of our film and a good focus has been put on it. The goal is to obtain a flexible substrate with good thermal conductivity for improving the power limitation of flexible electronic devices.

In order to further test the thermal robustness of the new film, thermogravimetric analysis (TGA) was performed in dry air environment, and the obtained mass loss curve is shown in Figure 64. The point of 5% mass loss (i.e. the point up to which the material remains stable) is measured to be at ~520°C, which is in agreement to obtained values of pure PI[83].

To corroborate 3D-foam/PI's stability up to 500°C, its electrical conductivity was measured after heating the sample up to 500°C for one hour. The film remained stable with $\rho \approx 1.3$ GΩ.cm (3DBN/PI case).

This further indicates that the 3D foam/PI films will remain operational and with improved thermal performance up to 500°C, which is 300°C beyond common operation temperatures of current electronic devices)[84].

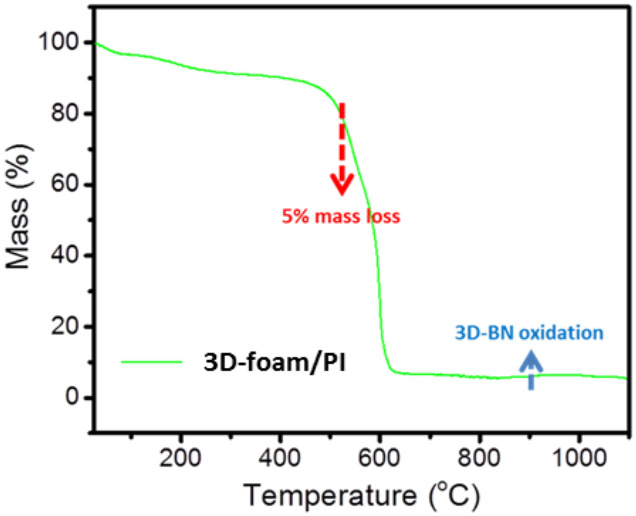

Figure 64: TGA thermal stability of 3D-BN/PI

Figure 65 shows obtained results of thermal conductivity (measured using Laser Flash Apparatus LINSEIS XFA 500) for the 3D foam/PI film, which clearly highlights the extreme increase in thermal conductivity obtained. For reference, the typical thermal conductivity of pure PI is demarcated (0.15 W/mK). The thermal conductivity of hybridized PI with a filling fraction of 0.3 vol% (0.35 wt%) of 3D-foam is in the order of 5 W.m^{-1}.K^{-1} throughout the tested temperature range, which corresponds to a 25 time increase.

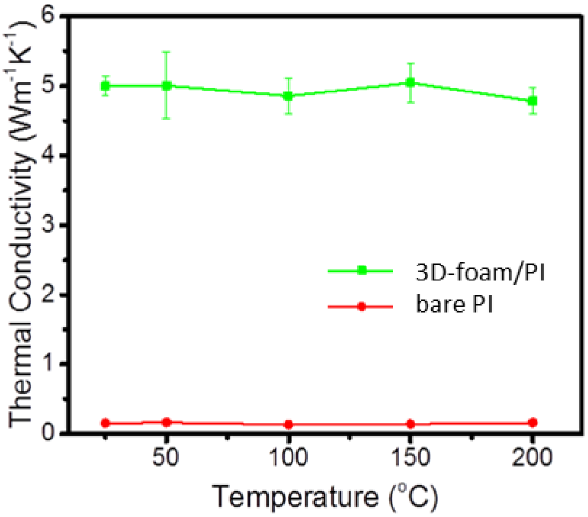

Figure 65: Laser Flash thermal conductivity result of 3D-foam/PI

For comparison, Table 1 tabulates the thermal conductivity enhancement of PI with 3D-C and other reported fillers, such as graphene[85] or other metal particles[86],[87]. For PI, the highest reported thermal conductivity was achieved with 45 vol% of silver particles, yielding 15 W.m^{-1}.K^{-1}.41 Taking into consideration that the result obtained here with 3D-C is only through a 0.3 vol% filling fraction, and in order to have a better comparison, the average improvement of the thermal conductivity per filling fraction of various fillers are also presented in Table 7.

We can see our substrate present a similar or higher thermal conductivity compared to other works, except from the work of Murakami et. al[86]. However, it has to be noticed that the authors used a filled volume of 45 vol%, which is very high compared to this work (0.3 vol%).

nanofiller	Thermal conductivity (W.m^{-1}.K^{-1})		Reference
	Bare PI	Filled PI	
SiC nanowires on graphene	0.25	0.577	[85]
Silver particles	0.2	15	[86]
Aluminum nitride	0.22	0.6	[87]
BN	0.18	1.2	[88]
3DC	**0.15**	**5**	**This work**

Table 7: comparison of thermal conductivity of different composites

a) First generation of substrates

To demonstrate the improved heat spreading capability achieved through the increase in thermal conductivity, test structures were deposited on both the hybridized and bare PI films. For this, conventional PI film and 3D-C/PI film were first coated with parylene (to avoid short circuits from the conductive 3D-C) and subsequently covered with thin lines of Ni/Au (110/90nm) via evaporation method using a mechanical mask, as shown in Figure 66. Subsequently, a voltage ramp was led through the test structures with two thin tips separated with a distance of 1000 and 2000µm and we observed the generated heat under infrared thermal camera at each step.

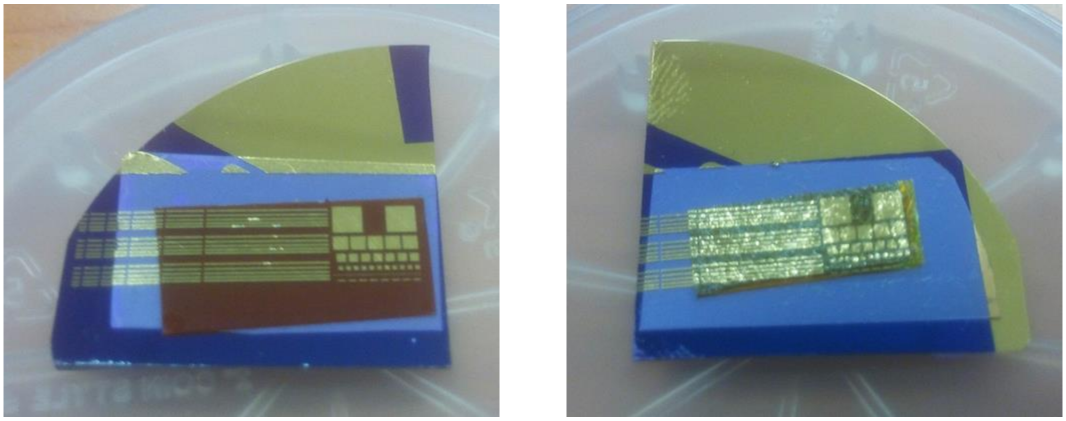

Figure 66: optical images of metallic lines deposited on commercial Kapton and 3DC/PI

Figure 67 shows the thermal images of both samples at 1.1 V. Beyond this point, the conventional PI sample breaks down, which means the maximum current applicable on PI is of ~180 mA and the maximum power supported is of ~0.2 mW. By direct comparison of the two samples at this point, it can be clearly seen that the heat generation on the conventional PI is significantly higher than on the hybridized film (it reaches up to 172°C).

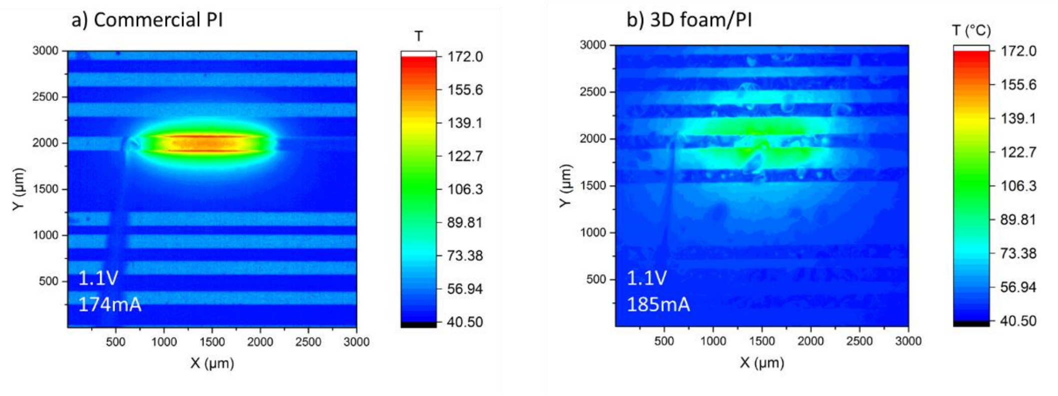

Figure 67: Thermal images of a) conventional PI and b) 3D foam/PI

The current was further ramped up on the 3D-foam/PI sample until reaching its breakdown. Figure 68 shows the obtained thermal image at maximum power. At this point, maximum temperatures of 180°C are reached on some spots. The 3D-foam/PI helped to increase the maximum current applicable to ~216 mA for 1.4V, which means a maximum power of ~0.3 mW, corresponding to a 50% improvement.

It must be noted that the thickness varied between samples (125 µm PI and 160 µm 3D-C/PI), as well as the roughness, which means after further process improvement, 3D-C/PI could even further improve performance. Indeed, the very rough surface of the samples of 1st generation lead to local spots with a high temperature compared to the rest of the surface which induce the breakdown of our metallic structure with the thickness used.

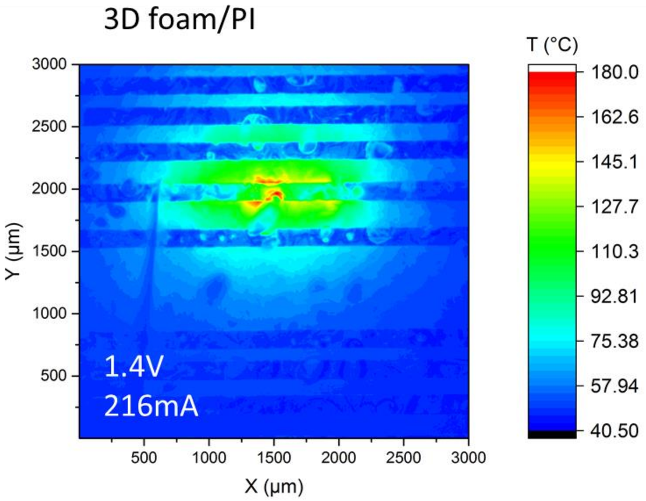

Figure 68: Thermal images of the 3D foam/PI at 1.4V and 216mA

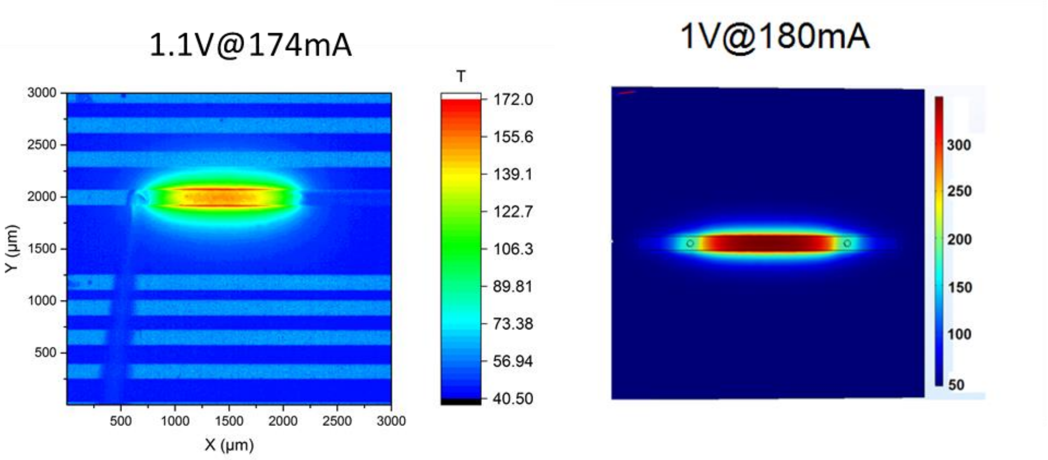

Figure 69: Comparison of the temperature mapping between measurements and simulation

A simulation of the temperature mapping has been performed using COMSOL. The dimensions, emissivity of the material and thickness were the same. We obtained a simulation in a qualitative agreement with the measurements, as we can see in Figure 69. The differences of the values of temperature can be explained by the difference of the emissivity at different temperatures and can be slightly changed by the presence of convection and radiation. Also, if we look at the profile temperature of a metallic line on Kapton in Figure 70, we can see that the distance α that needs the material to regain the temperature of the chuck (50°C) is really close to the thickness of the film, as expected for isotropic materials.

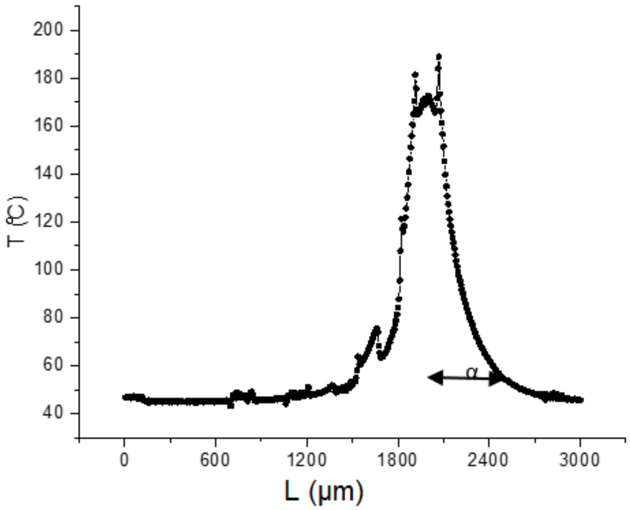

Figure 70: Profile temperature of commercial PI

Figure 71 shows the difference of emissivity of a test structure before and after the measurement. In this case we applied a voltage up to 1.2V for a current of 161mA before the break of the metallic structure. It can be clearly seen that the break of the metallic lines occurs at the middle of the test structure at a local point, resulting in an emissivity much higher in the damaged region, leading in an absence of electrical contact after this order of magnitude. We can assume that the roughness of the samples results in local point with higher temperature, resulting in the break of the metallic lines.

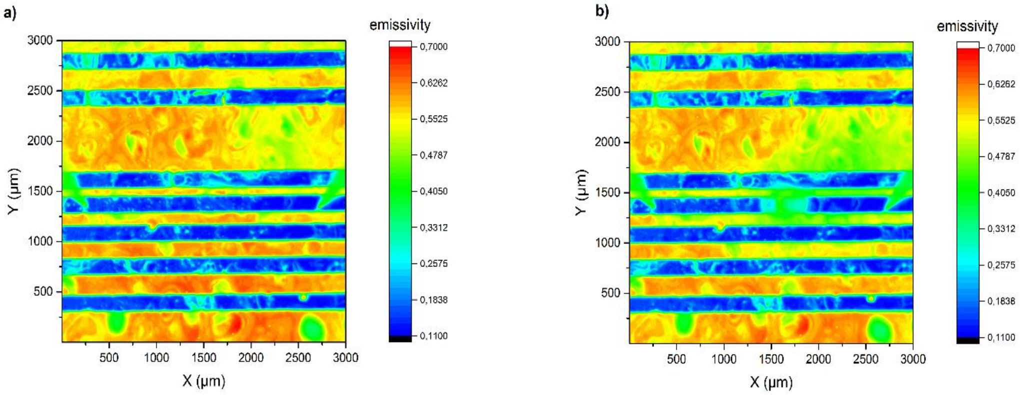

Figure 71: Difference of emissivity a) before the measurement and b) after the breaks of the line

b) Second generation of substrates

We deposited the same metallic lines on the samples of second generation and we performed the thermal characterization again to validate the ameliorations of the 2nd generation process. We achieved a maximum power of ~0.4mW before the break of the metallic lines, which corresponds to an amelioration of 100% compared to commercial PI and a 33% amelioration compared to the 1st generation samples. Indeed, the flatness of theses samples eliminated the presence of local high temperature spots induced by the roughness of the substrate, and the filling of PI with 3D foam allows a better thermal dissipation in the films.

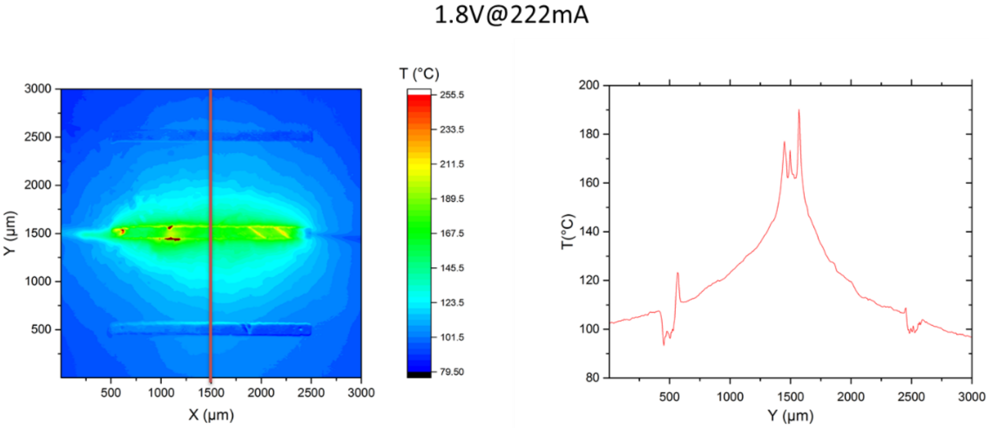

Figure 72: Temperature profile of the 3DC/PI of 2nd generation and associated profile

4) Dielectric constant measurement

In order to validate the use of our samples as dielectric substrate for high frequency devices (in the case of 3DBN/PI), we decided to fabricate some coplanar waveguide (CPW), to measure its dielectric constant and loss. A schematic of a CPW can be found in Figure 73. CPW is a transmission line which can be used to convey microwave frequency signals. It consists of a central conductive line deposited on the dielectric substrate with a width W, with a pair of two return conductors, or ground plane placed on each side of the conductive line, separated by a small gap S. Both lines have the same thickness t and the same length L. The length is quite higher than the separating gap S, which let one consider these lines as semi-infinite planes.

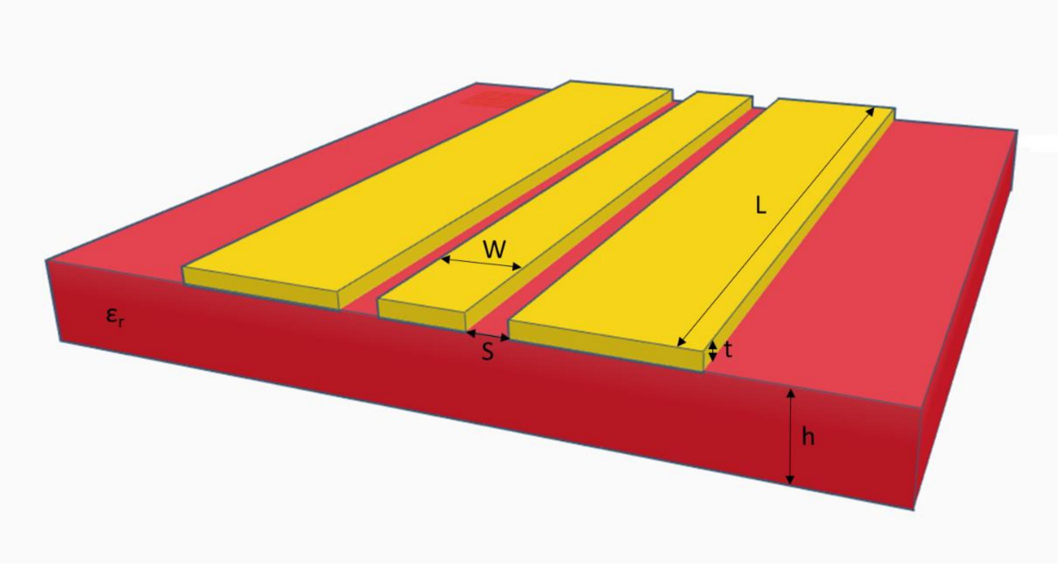

Figure 73: Schematic of a CPW transmission line

We decided to design CPWs with different size to obtain different impedances in order to obtain accurate results. We decided to use the dimensions W/S 60/10, 60/20 and 40/20µm which corresponds to 60, 73 and 81Ω impedances respectively (assuming that our samples have a dielectric constant close to the dielectric constant of pure PI). We decided to fabricate the CPWs using laser lithography, which is compatible with the dimensions required. A schematic of the process used can be found in Figure 74. We proceed to the deposition of 2µm of photolithography resist (b), the exposure of the resist with a UV laser (c), the development of the resist with an appropriate developer(d) and a metallization of 40/400nm of Ni/Au (e), followed by a classical lift-off of the samples (f).

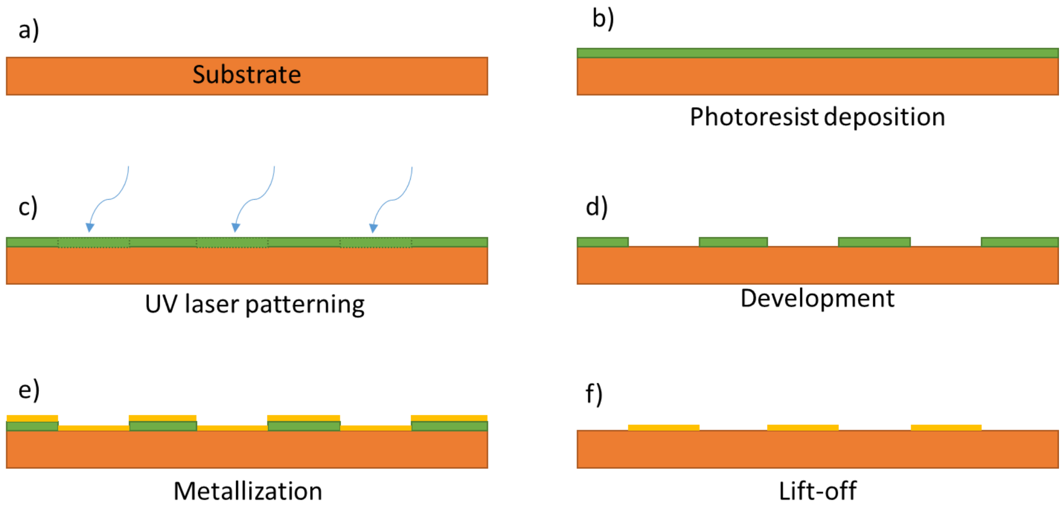

Figure 74: Schematic of the process used for the deposition of CPW lines

The first tentative of such a process have failed during the Lift-off step, leading to too few metallic lines, preventing us from performing the measurement. This can be explained by the poor adhesion of the metallic lines on the surface of the substrate, which can be explained by the roughness of the surface. Future investigations need to be done for a better adhesion of the metal on the surface for such a realization.

IV) Conclusion

In this chapter we demonstrated the process to achieve flexible substrates with enhanced thermal dissipation. We developed a technique to achieve a composite substrate composed with 3DC or 3DBN filled by PI through two generations of substrates. We showed that our substrates have a thermal conductivity around $5W.m^{-1}.K^{-1}$ with a thermal stability up to 500°C. We showed that the 3D foam matrix does not affect the mechanical properties of our samples with a good flexibility, and the 2nd generation of samples showed a limited roughness, making it compatible with standard microelectronic processes. We demonstrated the ability of our samples to evacuate the heat generated by thermistors on its surface with an improvement of 100% of maximum power applied compared to commercial PI. We designed and fabricated CPW transmission lines using laser lithography in order to obtain the dielectric constant and the loss of 3DBN/PI in the goal of making it compatible with high frequency electronics.

General conclusion

The growth of large area graphene and h-BN of good quality is a great challenge for research on 2D materials. Their properties are remarkable, but science is facing technological issues in the synthesis of these two materials, especially for h-BN, which has been studied later than graphene. One of the most efficient and cost-effective way to produce this type of materials is the use of CVD using metallic catalysts. In that goal we succeed in producing polycrystalline graphene on copper with quite a good quality, fully covering the metallic substrate with a size of 2x2cm. We tried to grow monocrystalline graphene using standard CVD and achieved hexagonal single crystals of 30µm, which is quite small compared to other methods used in literature. We synthetized polycrystalline h-BN using copper as a catalyst and ammonia borane as the precursor with a size of 6x2cm with a good homogeneity on all available substrate. We were able to transfer both graphene an h-BN on $Si0_2$ substrate using both classical wet transfer and bubbling transfer, leading to a fastest transfer and resulting on clean transfer of our materials, free of cracks, bubbles and resist residues, as optical images, SEM and Raman spectroscopy showed.

We succeed in producing both 3D graphene and 3D h-BN as foam using a Nickel foam as the catalyst, resulting in multilayer graphene and h-BN with a good quality. We produced new flexible and thermal efficient substrates using these foams as a filler in a matrix of PI, already commonly used as a classical flexible substrate for microelectronics. We developed two generations of substrates. We found similar mechanical properties and thermal stability as the commercial Kapton. We deposited thermistors on the surface in order to study the thermal dissipation of our samples. We improved the maximum power applied on the thermistors up to 100% before breakdown.

List of abbreviations

- 2D: two dimensional
- h-BN: hexagonal boron nitride
- RFID: radio frequency identification
- PEN: polyethylene naphthalate
- PET: polyethylene terephthalate
- PI: polyimide
- 3D: three dimensional
- CVD: chemical vapor deposition
- GFET: graphene field effect transistor
- SEM: scanning electron microscopy
- AFM: atomic force microscopy
- FWHM: full width at half maximum
- PMMA: Poly(Methyl MethAcrylate)
- UV: ultraviolet
- IPA: isopropyl alcohol
- APCVD: atmospheric pressure chemical vapor deposition
- XPS: X-ray photoelectron spectroscopy
- NMP: N-Méthyl-2-pyrrolidone
- RMS: root mean square
- VRH: variable range hopping
- CNT: carbon nanotube
- TGA: thermogravimetric analysis
- CPW: coplanar waveguide

References

[1] Castro Neto, A. H. , Guinea, F. , Peres, N. M. R. , Novoselov, K. S. , and Geim, A. K. The electronic properties of graphene. *Reviews of Modern Physics* **2009**, 81, 109–162.

[2] Mattevi, C. , Kim, H. , and Chhowalla, M. A review of chemical vapour deposition of graphene on copper. *Journal of Materials Chemistry* **2011**, 21, 3324–3334.

[3] Allen, M. J. , Tung, V. C. , and Kaner, R. B. Honeycomb Carbon: A Review of Graphene. *Chemical Reviews* **2010**, 110, 132–145.

[4] Ferrari, A. C. , Bonaccorso, F. , Fal'ko, V. , Novoselov, K. S. , Roche, S. , Bøggild, P. , Borini, S. , Koppens, F. H. L. , Palermo, V. , Pugno, N. , Garrido, J. A. , Sordan, R. , Bianco, A. , Ballerini, L. , Prato, M. , Lidorikis, E. , Kivioja, J. , Marinelli, C. , Ryhänen, T. , Morpurgo, A. , Coleman, J. N. , Nicolosi, V. , Colombo, L. , Fert, A. , Garcia-Hernandez, M. , Bachtold, A. , Schneider, G. F. , Guinea, F. , Dekker, C. , Barbone, M. , Sun, Z. , Galiotis, C. , Grigorenko, A. N. , Konstantatos, G. , Kis, A. , Katsnelson, M. , Vandersypen, L. , Loiseau, A. , Morandi, V. , Neumaier, D. , Treossi, E. , Pellegrini, V. , Polini, M. , Tredicucci, A. , Williams, G. M. , Hong, B. H. , Ahn, J.-H. , Kim, J. M. , Zirath, H. , Wees, B. J. van , Zant, H. van der , Occhipinti, L. , Matteo, A. D. , Kinloch, I. A. , Seyller, T. , Quesnel, E. , Feng, X. , Teo, K. , Rupesinghe, N. , Hakonen, P. , Neil, S. R. T. , Tannock, Q. , Löfwander, T. , and Kinaret, J. Science and technology roadmap for graphene, related two-dimensional crystals, and hybrid systems. *Nanoscale* **2015**, 7, 4598–4810.

[5] Bolotin, K. I. , Sikes, K. J. , Jiang, Z. , Klima, M. , Fudenberg, G. , Hone, J. , Kim, P. , and Stormer, H. L. Ultrahigh electron mobility in suspended graphene. *Solid State Communications* **2008**, 146, 351–355.

[6] Balandin, A. A. , Ghosh, S. , Bao, W. , Calizo, I. , Teweldebrhan, D. , Miao, F. , and Lau, C. N. Superior Thermal Conductivity of Single-Layer Graphene. *Nano Letters* **2008**, 8, 902–907.

[7] Sharma, B. K. and Ahn, J.-H. Graphene based field effect transistors: Efforts made towards flexible electronics. *Solid-State Electronics* **2013**, 89, 177–188.

[8] Wallace, P. R. The Band Theory of Graphite. *Physical Review* **1947**, 71, 622–634.

[9] Novoselov, K. S. , Geim, A. K. , Morozov, S. V. , Jiang, D. , Zhang, Y. , Dubonos, S. V. , Grigorieva, I. V. and , and Firsov, A. A. Electric field effect in atomically thin carbon films. *science* **2004**, 306, 666–669.

[10] Pakdel, A. , Bando, Y. , and Golberg, D. Nano boron nitride flatland. *Chemical Society Reviews* **2014**, 43, 934–959.

[11] Liu, P. , Sherman, E. , and Jacobsen, A. Design and fabrication of multifunctional structural batteries. *Journal of Power Sources* **2009**, 189, 646–650.

[12] Jung, M. , Kim, J. , Noh, J. , Lim, N. , Lim, C. , Lee, G. , Kim, J. , Kang, H. , Jung, K. , Leonard, A. D. , Tour, J. M. , and Cho, G. All-Printed and Roll-to-Roll-Printable 13.56-MHz-Operated 1-bit RF Tag on Plastic Foils. *IEEE Transactions on Electron Devices* **2010**, 57, 571–580.

[13] Radivojevic, Z., Beecher, P., Bower, C., Haque, S., Andrew, P., Hasan, T., Bonaccorso, F., Ferrari, A. C., and Henson, B. *In Electrotactile Touch Surface by Using Transparent Graphene*, New York, NY, USA, ACM: New York, NY, USA, 2012.

[14] Bae, S. , Kim, H. , Lee, Y. , Xu, X. , Park, J.-S. , Zheng, Y. , Balakrishnan, J. , Lei, T. , Ri Kim, H. , Song, Y. I. , Kim, Y.-J. , Kim, K. S. , Özyilmaz, B. , Ahn, J.-H. , Hong, B. H. , and Iijima, S. Roll-to-roll production of 30-inch graphene films for transparent electrodes. *Nature Nanotechnology* **2010**, 5, 574–578.

[15] Zou, L. , Wang, L. , Wu, Y. , Ma, C. , Yu, S. , and Liu, X. Trends Analysis of Graphene Research and Development. *Journal of Data and Information Science* **2018**, 3, 82–100.

[16] Bonaccorso, F. , Sun, Z. , Hasan, T. , and Ferrari, A. C. Graphene photonics and optoelectronics. *Nature Photonics* **2010**, 4, 611–622.

[17] Lee, C. , Wei, X. , Kysar, J. W. , and Hone, J. Measurement of the elastic properties and intrinsic strength of monolayer graphene. *Science (New York, N.Y.)* **2008**, 321, 385–388.

[18] Nair, R. R. , Blake, P. , Grigorenko, A. N. , Novoselov, K. S. , Booth, T. J. , Stauber, T. , Peres, N. M. R. , and Geim, A. K. Fine structure constant defines visual transparency of graphene. *Science (New York, N.Y.)* **2008**, 320, 1308.

[19] Balmain, W. H. Bemerkungen über die Bildung von Verbindungen des Bors und Siliciums mit Stickstoff und gewissen Metallen. *Journal für Praktische Chemie* **1842**, 27, 422–430.

[20] Watanabe, K. and Taniguchi, T. Hexagonal Boron Nitride as a New Ultraviolet Luminescent Material and Its Application. *International Journal of Applied Ceramic Technology* **2011**, 8, 977–989.

[21] Watanabe, K. , Taniguchi, T. , and Kanda, H. Direct-bandgap properties and evidence for ultraviolet lasing of hexagonal boron nitride single crystal. *Nature Materials* **2004**, 3, 404–409.

[22] Sung, C.-M. and Tai, M.-F. Reactivities of transition metals with carbon: Implications to the mechanism of diamond synthesis under high pressure. *International Journal of Refractory Metals and Hard Materials* **1997**, 15, 237–256.

[23] Batzill, M. The surface science of graphene: Metal interfaces, CVD synthesis, nanoribbons, chemical modifications, and defects. *Surface Science Reports* **2012**, 67, 83–115.

[24] Li, X. , Cai, W. , An, J. , Kim, S. , Nah, J. , Yang, D. , Piner, R. , Velamakanni, A. , Jung, I. , Tutuc, E. , Banerjee, S. K. , Colombo, L. , and Ruoff, R. S. Large-Area Synthesis of High-Quality and Uniform Graphene Films on Copper Foils. *Science* **2009**, 324, 1312–1314.

[25] Chen, X. , Zhang, L. , and Chen, S. Large area CVD growth of graphene. *Synthetic Metals* **2015**, 210, 95–108.

[26] Weatherup, R. S. , Bayer, B. C. , Blume, R. , Baehtz, C. , Kidambi, P. R. , Fouquet, M. , Wirth, C. T. , Schlögl, R. , and Hofmann, S. On the Mechanisms of Ni-Catalysed Graphene Chemical Vapour Deposition. *ChemPhysChem* **2012**, 13, 2544–2549.

[27] Weatherup, R. S. , Bayer, B. C. , Blume, R. , Ducati, C. , Baehtz, C. , Schlögl, R. , and Hofmann, S. In Situ Characterization of Alloy Catalysts for Low-Temperature Graphene Growth. *Nano Letters* **2011**, 11, 4154–4160.

[28] Yu, Q. , Lian, J. , Siriponglert, S. , Li, H. , Chen, Y. P. , and Pei, S.-S. Graphene segregated on Ni surfaces and transferred to insulators. *Applied Physics Letters* **2008**, 93, 113103.

[29] Simsek, E. and Mukherjee, B. Visibility of atomically-thin layered materials buried in silicon dioxide. *Nanotechnology* **2015**, 26, 455701.

[30] Zhu, F.-Y. , Wang, Q.-Q. , Zhang, X.-S. , Hu, W. , Zhao, X. , and Zhang, H.-X. 3D nanostructure reconstruction based on the SEM imaging principle, and applications. *Nanotechnology* **2014**, 25, 185705.

[31] Raman, C. V. and Krishnan, K. S. A New Type of Secondary Radiation. *Nature* **1928**, 121, 501–502.

[32] Wang, Y. , Alsmeyer, D. C. , and McCreery, R. L. Raman spectroscopy of carbon materials: structural basis of observed spectra. *Chemistry of Materials* **1990**, 2, 557–563.

[33] Ferrari, A. C. and Basko, D. M. Raman spectroscopy as a versatile tool for studying the properties of graphene. *Nature Nanotechnology* **2013**, 8, 235–246.

[34] Malard, L. M. , Pimenta, M. A. , Dresselhaus, G. , and Dresselhaus, M. S. Raman spectroscopy in graphene. *Physics Reports* **2009**, 473, 51–87.

[35] Basko, D. M. , Piscanec, S. , and Ferrari, A. C. Electron-electron interactions and doping dependence of the two-phonon Raman intensity in graphene. *Physical Review B* **2009**, 80, 165413.

[36] Casiraghi, C. , Hartschuh, A. , Qian, H. , Piscanec, S. , Georgi, C. , Fasoli, A. , Novoselov, K. S. , Basko, D. M. , and Ferrari, A. C. Raman Spectroscopy of Graphene Edges. *Nano Letters* **2009**, 9, 1433–1441.

[37] Chen, Z. , Ren, W. , Liu, B. , Gao, L. , Pei, S. , Wu, Z.-S. , Zhao, J. , and Cheng, H.-M. Bulk growth of mono- to few-layer graphene on nickel particles by chemical vapor deposition from methane. *Carbon* **2010**, 48, 3543–3550.

[38] Al-Mumen, H. , Rao, F. , Li, W. , and Dong, L. Singular Sheet Etching of Graphene with Oxygen Plasma. *Nano-Micro Letters* **2014**, 6, 116–124.

[39] Miseikis, V.; Xiang, S.; Roddaro, S.; Heun, S.; and Coletti, C. Perfecting the Growth and Transfer of Large Single-Crystal CVD Graphene: A Platform Material for Optoelectronic Applications. *In GraphITA*; Springer, Cham, 2017; pp. 113–124.

[40] Suhail, A. , Islam, K. , Li, B. , Jenkins, D. , and Pan, G. Reduction of polymer residue on wet–transferred CVD graphene surface by deep UV exposure. *Applied Physics Letters* **2017**, 110, 183103.

[41] Xia, M. , Su, Z. , and Zhang, S. Raman spectra of bilayer graphene covered with Poly(methyl methacrylate) thin film. *AIP Advances* **2012**, 2, 032122.

[42] Wei, D. and Liu, Y. Controllable Synthesis of Graphene and Its Applications. *Advanced Materials* **2010**, 22, 3225–3241.

[43] Yu, Q. , Jauregui, L. A. , Wu, W. , Colby, R. , Tian, J. , Su, Z. , Cao, H. , Liu, Z. , Pandey, D. , Wei, D. , Chung, T. F. , Peng, P. , Guisinger, N. P. , Stach, E. A. , Bao, J. , Pei, S.-S. , and Chen, Y. P. Control and characterization of individual grains and grain boundaries in graphene grown by chemical vapour deposition. *Nature Materials* **2011**, 10, 443–449.

[44] Zhou, H. , Yu, W. J. , Liu, L. , Cheng, R. , Chen, Y. , Huang, X. , Liu, Y. , Wang, Y. , Huang, Y. , and Duan, X. Chemical vapour deposition growth of large single crystals of monolayer and bilayer graphene. *Nature Communications* **2013**, 4, 2096.

[45] Gao, L. , Ren, W. , Xu, H. , Jin, L. , Wang, Z. , Ma, T. , Ma, L.-P. , Zhang, Z. , Fu, Q. , Peng, L.-M. , Bao, X. , and Cheng, H.-M. Repeated growth and bubbling transfer of graphene with millimetre-size single-crystal grains using platinum. *Nature Communications* **2012**, 3, 699.

[46] Yan, Z. , Lin, J. , Peng, Z. , Sun, Z. , Zhu, Y. , Li, L. , Xiang, C. , Samuel, E. L. , Kittrell, C. , and Tour, J. M. Toward the Synthesis of Wafer-Scale Single-Crystal Graphene on Copper Foils. *ACS Nano* **2012**, 6, 9110–9117.

[47] Vlassiouk, I. , Regmi, M. , Fulvio, P. , Dai, S. , Datskos, P. , Eres, G. , and Smirnov, S. Role of Hydrogen in Chemical Vapor Deposition Growth of Large Single-Crystal Graphene. *ACS Nano* **2011**, 5, 6069–6076.

[48] Li, X. , Magnuson, C. W. , Venugopal, A. , Tromp, R. M. , Hannon, J. B. , Vogel, E. M. , Colombo, L. , and Ruoff, R. S. Large-Area Graphene Single Crystals Grown by Low-Pressure Chemical Vapor Deposition of Methane on Copper. *Journal of the American Chemical Society* **2011**, 133, 2816–2819.

[49] Yoon, S.-M. , Choi, W. M. , Baik, H. , Shin, H.-J. , Song, I. , Kwon, M.-S. , Bae, J. J. , Kim, H. , Lee, Y. H. , and Choi, J.-Y. Synthesis of Multilayer Graphene Balls by Carbon Segregation from Nickel Nanoparticles. *ACS Nano* **2012**, 6, 6803–6811.

[50] Ni Foam - Product Detail - Latech - Singapore Leading Lab Consumable Supplier. http://www.latech.com.sg/product/1423718970-Ni+Foam.html (accessed Nov. 13, 2017).

[51] Chen, Z. , Ren, W. , Gao, L. , Liu, B. , Pei, S. , and Cheng, H.-M. Three-dimensional flexible and conductive interconnected graphene networks grown by chemical vapour deposition. *Nature Materials* **2011**, 10, nmat3001.

[52] Loeblein, M. , Bolker, A. , Tsang, S. H. , Atar, N. , Uzan-Saguy, C. , Verker, R. , Gouzman, I. , Grossman, E. , and Teo, E. H. T. 3D Graphene-Infused Polyimide with Enhanced Electrothermal Performance for Long-Term Flexible Space Applications. *Small* **2015**, 11, 6425–6434.

[53] Geim, A. K. and Novoselov, K. S. The rise of graphene. *Nature Materials* **2007**, 6, 183–191.

[54] Whittell, G. R. and Manners, I. Advances with Ammonia-Borane: Improved Recycling and Use as a Precursor to Atomically Thin BN Films. *Angewandte Chemie International Edition* **2011**, 50, 10288–10289.

[55] Guo, N. , Wei, J. , Fan, L. , Jia, Y. , Liang, D. , Zhu, H. , Wang, K. , and Wu, D. Controllable growth of triangular hexagonal boron nitride domains on copper foils by an improved low-pressure chemical vapor deposition method. *Nanotechnology* **2012**, 23, 415605.

[56] Preobrajenski, A. B. , Vinogradov, A. S. , and Mårtensson, N. Monolayer of h-BN chemisorbed on Cu(111) and Ni(111): The role of the transition metal 3d states. *Surface Science* **2005**, 582, 21–30.

[57] Kim, K. K. , Hsu, A. , Jia, X. , Kim, S. M. , Shi, Y. , Hofmann, M. , Nezich, D. , Rodriguez-Nieva, J. F. , Dresselhaus, M. , Palacios, T. , and Kong, J. Synthesis of Monolayer Hexagonal Boron Nitride on Cu Foil Using Chemical Vapor Deposition. *Nano Letters* **2012**, 12, 161–166.

[58] Kim, K. K. , Lee, H. S. , and Lee, Y. H. Synthesis of hexagonal boron nitride heterostructures for 2D van der Waals electronics. *Chemical Society Reviews* **2018**, 47, 6342–6369.

[59] Song, X. , Gao, J. , Nie, Y. , Gao, T. , Sun, J. , Ma, D. , Li, Q. , Chen, Y. , Jin, C. , Bachmatiuk, A. , Rümmeli, M. H. , Ding, F. , Zhang, Y. , and Liu, Z. Chemical vapor deposition growth of large-scale hexagonal boron nitride with controllable orientation. *Nano Research* **2015**, 8, 3164–3176.

[60] Han, G. H. , Rodríguez-Manzo, J. A. , Lee, C.-W. , Kybert, N. J. , Lerner, M. B. , Qi, Z. J. , Dattoli, E. N. , Rappe, A. M. , Drndic, M. , and Johnson, A. T. C. Continuous Growth of Hexagonal Graphene and Boron Nitride In-Plane Heterostructures by Atmospheric Pressure Chemical Vapor Deposition. *ACS Nano* **2013**, 7, 10129–10138.

[61] Gorbachev, R. V. , Riaz, I. , Nair, R. R. , Jalil, R. , Britnell, L. , Belle, B. D. , Hill, E. W. , Novoselov, K. S. , Watanabe, K. , Taniguchi, T. , Geim, A. K. , and Blake, P. Hunting for Monolayer Boron Nitride: Optical and Raman Signatures. *Small* **2011**, 7, 465–468.

[62] Li, L. H. and Chen, Y. Atomically Thin Boron Nitride: Unique Properties and Applications. *Advanced Functional Materials* **2016**, 26, 2594–2608.

[63] Koepke, J. C. , Wood, J. D. , Chen, Y. , Schmucker, S. W. , Liu, X. , Chang, N. N. , Nienhaus, L. , Do, J. W. , Carrion, E. A. , Hewaparakrama, J. , Rangarajan, A. , Datye, I. , Mehta, R. , Haasch, R. T. , Gruebele, M. , Girolami, G. S. , Pop, E. , and Lyding, J. W. Role of Pressure in the Growth of Hexagonal Boron Nitride Thin Films from Ammonia-Borane. *Chemistry of Materials* **2016**, 28, 4169–4179.

[64] Ito, S. , Rothenberger, G. , Liska, P. , Comte, P. , Zakeeruddin, S. M. , Péchy, P. , Nazeeruddin, M. K. , and Grätzel, M. High-efficiency (7.2%) flexible dye-sensitized solar cells with Ti-metal substrate for nanocrystalline-TiO 2 photoanode. *Chemical Communications* **2006**, 4004–4006.

[65] Gustafsson, G. , Cao, Y. , Treacy, G. M. , Klavetter, F. , Colaneri, N. , and Heeger, A. J. Flexible light-emitting diodes made from soluble conducting polymers. *Nature* **1992**, 357, 477–479.

[66] Könenkamp, R. , Word, R. C. , and Schlegel, C. Vertical nanowire light-emitting diode. *Applied Physics Letters* **2004**, 85, 6004–6006.

[67] Someya, T. , Sekitani, T. , Iba, S. , Kato, Y. , Kawaguchi, H. , and Sakurai, T. A large-area, flexible pressure sensor matrix with organic field-effect transistors for artificial skin applications. *Proceedings of the National Academy of Sciences of the United States of America* **2004**, 101, 9966–9970.

[68] Feger, C. Advances in Polyimide: Science and Technology. CRC Press: 1993.

[69] Sun, Y. and Rogers, J. A. Inorganic Semiconductors for Flexible Electronics. *Advanced Materials* **2007**, 19, 1897–1916.

[70] Cahill, D. G. and Pohl, R. O. Thermal conductivity of amorphous solids above the plateau. *Physical Review B* **1987**, 35, 4067–4073.

[71] Glassbrenner, C. J. and Slack, G. A. Thermal Conductivity of Silicon and Germanium from 3\ifmmode^\circ\else\textdegree\fi{}K to the Melting Point. *Physical Review* **1964**, 134, A1058–A1069.

[72] Du, J. and Cheng, H.-M. The Fabrication, Properties, and Uses of Graphene/Polymer Composites. *Macromolecular Chemistry and Physics* **2012**, 213, 1060–1077.

[73] Marconnet, A. M. , Panzer, M. A. , and Goodson, K. E. Thermal conduction phenomena in carbon nanotubes and related nanostructured materials. *Reviews of Modern Physics* **2013**, 85, 1295–1326.

[74] Ebadi-Dehaghani, H. and Nazempour, M. Thermal Conductivity of Nanoparticles Filled Polymers. **2012**

[75] Moore, A. L. and Shi, L. Emerging challenges and materials for thermal management of electronics. *Materials Today* **2014**, 17, 163–174.

[76] Nam, K.-H. , Seo, J. , Seo, K. , Jang, W. , and Han, H. Residual stress behavior and physical properties of transparent polyimide/surface-modified CaCO3 nanocomposite films. *Macromolecular Research* **2014**, 22, 669–677.

[77] Atar, N. , Grossman, E. , Gouzman, I. , Bolker, A. , and Hanein, Y. Reinforced Carbon Nanotubes as Electrically Conducting and Flexible Films for Space Applications. *ACS Applied Materials & Interfaces* **2014**, 6, 20400–20407.

[78] Petrone, N. , Chari, T. , Meric, I. , Wang, L. , Shepard, K. L. , and Hone, J. Flexible Graphene Field-Effect Transistors Encapsulated in Hexagonal Boron Nitride. *ACS nano* **2015**, 9, 8953–8959.

[79] Jang, H. , Park, Y. J. , Chen, X. , Das, T. , Kim, M.-S. , and Ahn, J.-H. Graphene-Based Flexible and Stretchable Electronics. *Advanced Materials* **2016**, 28, 4184–4202.

[80] Wei, W. , Pallecchi, E. , Haque, S. , Borini, S. , Avramovic, V. , Centeno, A. , Amaia, Z. , and Happy, H. Mechanically robust 39 GHz cut-off frequency graphene field effect transistors on flexible substrates. *Nanoscale* **2016**, 8, 14097–14103.

[81] Godet, C. Physics of bandtail hopping in disordered carbons. *Diamond and Related Materials* **2003**, 12, 159–165.

[82] Li, Q. W. , Li, Y. , Zhang, X. F. , Chikkannanavar, S. B. , Zhao, Y. H. , Dangelewicz, A. M. , Zheng, L. X. , Doorn, S. K. , Jia, Q. X. , Peterson, D. E. , Arendt, P. N. , and Zhu, Y. T. Structure-Dependent Electrical Properties of Carbon Nanotube Fibers. *Advanced Materials* **2007**, 19, 3358–3363.

[83] Ahmad, M. B. , Gharayebi, Y. , Salit, M. S. , Hussein, M. Z. , Ebrahimiasl, S. , and Dehzangi, A. Preparation, Characterization and Thermal Degradation of Polyimide (4-APS/BTDA)/SiO2 Composite Films. *International Journal of Molecular Sciences* **2012**, 13, 4860–4872.

[84] Tummala Fundamentals of Microsystems Packaging. McGraw Hill Professional: 2001.

[85] Dai, W. , Yu, J. , Liu, Z. , Wang, Y. , Song, Y. , Lyu, J. , Bai, H. , Nishimura, K. , and Jiang, N. Enhanced thermal conductivity and retained electrical insulation for polyimide composites with SiC nanowires grown on graphene hybrid fillers. *Composites Part A: Applied Science and Manufacturing* **2015**, 76, 73–81.

[86] Murakami, T. , Ebisawa, K. , Miyao, K. , and Ando, S. Enhanced Thermal Conductivity in Polyimide/Silver Particle Composite Films Based on Spontaneous Formation of Thermal Conductive Paths. *Journal of Photopolymer Science and Technology* **2014**, 27, 187–191.

[87] Xie, S.-H. , Zhu, B.-K. , Li, J.-B. , Wei, X.-Z. , and Xu, Z.-K. Preparation and properties of polyimide/aluminum nitride composites. *Polymer Testing* **2004**, 23, 797–801.

[88] Li, T.-L. and Hsu, S. L.-C. Enhanced Thermal Conductivity of Polyimide Films via a Hybrid of Micro- and Nano-Sized Boron Nitride. *The Journal of Physical Chemistry B* **2010**, 114, 6825–6829.

Scientific publications

Reliable bubbling transfer of CVD isolated large-hexagonal-domain graphene BEN SALK S., PHAM P.H.Q., LEVERT T., PALLECCHI E., BURKE P.J., HAPPY H.G. Graphene Week 2018, San Sebastian, Spain, September 10-14, 2018, paper Th-73

Annex

I. Growth and transfer of graphene and h-BN

Here are the several steps detailed for the transfer of graphene:

- Resist coating with PMMA 5% 950K with a speed of 3000rpm, acceleration of 1000rpm for 10s.
- Annealing using Sawatech oven 30 min from room temperature to 110°C, 30mn staying at 110°C, 30mn from 110°C to room temperature.
- Cleaning of the Becher using Piranha 2 H_2SO_4 for 1 H_2O_2.
- O_2 plasma etching of the back face using 50W, 100mTorr, 25sccm of O_2.
- Etching of copper foil using $(NH_4)_2S_2O_8$. $C = \frac{n}{V} = \frac{m}{\mu V}$ so $m = CV\mu = 222.2 \times 0.1 \times 0.2 = 4.56g$ for $100ml$
- Ozone treatment of the SiO_2/Si substrate for hydrophobic improvement for 10mn.
- 10 times rinsing of the PMMA/graphene with DI water.
- Transfer of the PMMA/graphene on the substrate
- Annealing using Sawatech oven 30 min from room temperature to 90°C, 30mn staying at 90°C, 30mn from 90°C to room temperature.
- Deep UV treatment for 30min at 500W.
- 2 baths of acetone at room temperature. 3rd bath of acetone for 30mn at 35°C. 1 bath of IPA then N_2 drying.

The only differences with the transfer of h-BN is the resist coating parameters which are a speed of 2000rpm, an acceleration of 1000rpm for 10s. Also, the plasma etching of the back face are provided with a Ar plasma with 100W, 100mTorr for 30 sccm of Ar.

II. Printed transistors

Transistors with a channel composed by graphene and carbon nanotubes inks (from Cambridge) have been fabricated in IEMN by PhD Wei Wei. We have printed transistors with graphene ink, with carbon nanotubes ink and both graphene and carbon nanotubes ink. These transistors have been fabricated with more or less ink by varying the number of passes during the printing fabrication. The following figure shows the structure of these transistors

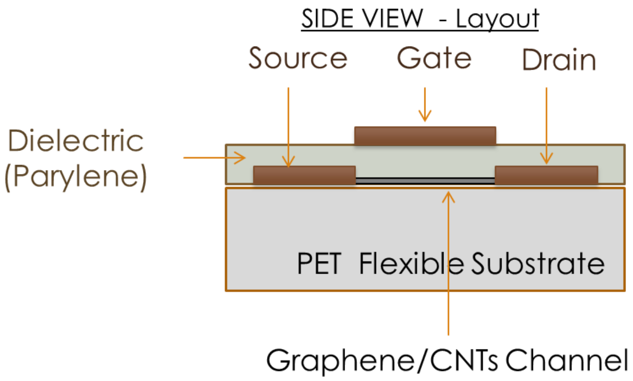

Figure 75: Structure of the printed transistors

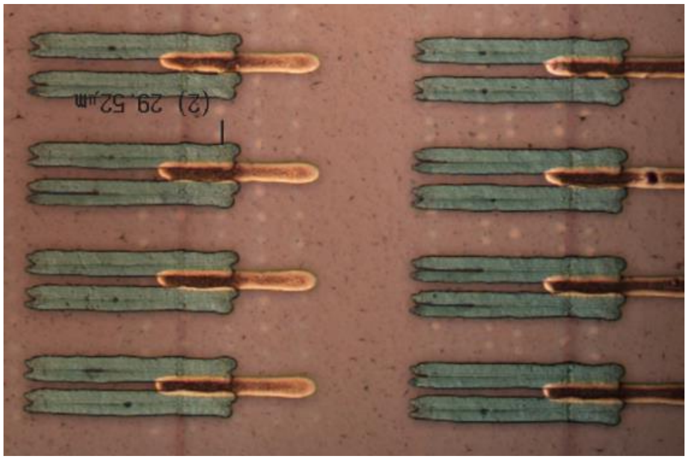

Figure 76: Optical image of the printed transistors

DC measurements have been realized on these transistors in order to extract principal characteristics such as contact resistance, channel resistance, mobility and density of the charge carriers. In this goal we realized a modelization work based on the transfer characteristics based on the following equations:

$$\sigma_{ch} = n_{tot}e\mu \text{ and } n_{tot} = \sqrt{n_0^2 + \left[\frac{C_g(V_g - V_D)}{e}\right]^2}$$

Moreover, we have:

$$I_{DS} = \sigma_{ch}\frac{W}{L_{DS}}V_{ch} \text{ with } V_{ch} = V_{DS} - 2R_C I_{DS}$$

These equations lead to the following one:

$$I_{DS} = \sigma_{ch}\frac{W}{L_{DS}}V_{DS} = \sqrt{n_0^2 + \left[\frac{C_g(V_g - V_D)}{e}\right]^2}\, e\mu\frac{W}{L_{DS}}V_{DS}$$

With σ_{ch} the conductivity of the channel, n_{tot} the total charge density, μ the mobility of the charge carriers n_0 the residual charge density, $C_g = \frac{\epsilon_0\epsilon_r}{d}$ the capacitance of the grid, V_g the grid tension, V_D the Dirac point, W the channel width, L_{DS} the source-drain distance.

$$I_{DS}^2 = n_0^2e^2\mu^2\frac{W^2}{L_{DS}^2}V_{ch}^2 + \frac{C_g^2\left(V_g - V_D\right)^2}{e^2}e^2\mu^2\frac{W^2}{L_{DS}^2}V_{ch}^2$$

$$I_{DS}^2 = \left(n_0e\mu\frac{W}{L_{DS}}V_{ch}\right)^2 + \left(\frac{C_g\mu W V_{ch}}{L_{DS}}\right)^2\left(V_g - V_D\right)^2$$

We can do a fitting of 2nd order of I_{DS}^2 as a function of $\left(V_g - V_D\right)$

$$I_{DS}^2 = p(1)\left(V_g - V_D\right)^2 + p(2)\left(V_g - V_D\right) + p(3)$$

$$\text{With } \left(\frac{C_g\mu W V_{ch}}{L_{DS}}\right)^2 = p(1) \text{ so } \boxed{\mu = \frac{L_{DS}}{C_g V_{ch} W}\sqrt{p(1)}}$$

$$p(2) = 0$$

$$\left(n_0 e\mu \frac{W}{L_{DS}} V_{ch}\right)^2 = p(3) \text{ so } \boxed{n_0 = \frac{L_{DS}}{e\mu W V_{ch}} \sqrt{p(3)}}$$

Based on this modelization, we could extract important information such as contact resistance, mobility of charge carriers, or density of charge as a function of the number of printing passes for the different inks. Figure 77 shows an example of the transfer characteristics measurements and the numerical modelization of a transistor composed of both graphene and carbon nanotubes ink with 15 passes of ink. Figure 78 sum up the results on all modelization made.

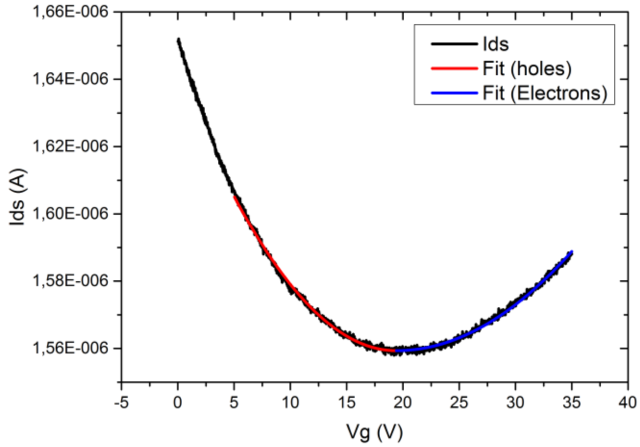

Figure 77: Transfer characteristics of a printed transistor with graphene and carbon nanotubes ink and numerical modelization

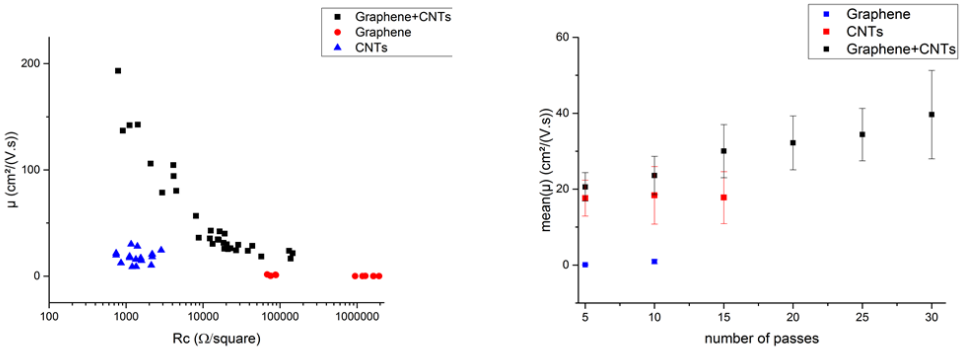

Figure 78: a) mobility and square resistance of the different inks b) Mobility as a function of the number of passes for the different inks used

Finally, the most performing ink seems to be the ink composed of both graphene and carbon nanotubes. Indeed, this ink showed the highest mobility of charge carriers with a linear tendency, with a higher density of charge carriers, with reasonable resistance similar to those of ink composed only with graphene or only with carbon nanotubes.

The following text is the script of the main fitting file using MATLAB.

```
%clear all
close all

%files
path = 'C:\Users\admin\Dropbox\PGFET1e2\TheoFITTING\data_to_fit\';
%parameters
h = 290e-9;
Rc=0;
W=35E-6;
eps_r = 3;
%constants
e=1.602E-19;
eps_0 = 8.854E-12;

%%%%%%%%%%%%%%%%%%%%%%%%%%%%%%%%%%%%%%%%%%%%%
liste=dir(path);
n=length(liste);


fin1=[];
fin2=[];
fin3=[];
error_mob=[];
error_n0=[];
```

```
for k=3:(n)

    nom=liste(k).name;
    tmp=importdata(strcat(path, nom), '\t',1);
    A = tmp.data;

    tmp = strread(nom,'%s','delimiter','_');
    tmp2 = tmp(5);
    tmp2 = tmp2{1};
    tmp3 = tmp(4);
    tmp3 = tmp3{1};

    nb_pass=str2num(tmp3(1:end-1));

    if (tmp2) == 'd1'
        Lds=29E-6;
    elseif tmp2 == 'd2'
        Lds=32E-6;
        elseif tmp2 == 'd3'
        Lds=36E-6;
        elseif tmp2 == 'd5'
        Lds=57E-6;
        elseif tmp2 == 'd6'
        Lds=66E-6;
    else
    Lds = 10000;
    'LDS not recognized, using 10Km, CHECK FILENAME'
    end



S=W*Lds;
Cg=(eps_0*eps_r*S)/(h);
Vds=A(:,3);
Ids=A(:,4);
Vg=A(:,1);
Vch=Vds-2*Rc*Ids;
[a,b]=min(Ids);
Vd=Vg(b);


%F = @(x,xdata)sqrt(x(1)+(Cg.*(xdata-
Vd)./(W*Lds*e)).^2).*e*x(2)*Lds/W.*Vch;
%x0=[1E24 50];
%DiffMinChange=1e-6;
%[x,resnorm,~,exitflag,output] = lsqcurvefit(F,x0,Vg,Ids);


x=Vg;
y=Ids.^2;
[p,S]=polyfit(x,y,2);
delta=sqrt(diag(inv(S.R)*inv(S.R')).*S.normr.^2./S.df);
%p
figure
plot(Vg,Ids,Vg,sqrt(p(3)+p(2)*Vg+p(1)*(Vg.^2)),'r')
title(nom)
xlabel('V_G(V)')
```

```
ylabel('I_D_S(A)')

mob1=sqrt(p(1)*W^4/(Cg^2*Vch(1)^2));
mob2=sqrt(-p(2)*W^4/(2*Cg^2*Vd*Vch(1)^2));
mob=(mob1+mob2)/2;
n0=sqrt((p(3)-
(Cg^2*Vd^2*Vch(1)^2*mob^2)/W^4)*W^2/(e^2*mob^2*Lds^2*Vch(1)^2));

%ecart_mob=[mob-delta(1)*W^2/(Cg^2*Vch(1)),
mob+delta(1)*W^2/(Cg^2*Vch(1))];
%ecart_n0=[n0-sqrt(abs((delta(3)-
(Cg^2*Vd^2*Vch(1)*mob)/W^2)*W/(e*mob*Lds*Vch(1)))),
n0+sqrt(abs((delta(3)-
(Cg^2*Vd^2*Vch(1)*mob)/W^2)*W/(e*mob*Lds*Vch(1))))];

fin1=[fin1;nb_pass,mob];
fin2=[fin2;nb_pass,n0];
fin3=[fin3;nb_pass,Vd];

error_mob1=(delta(1)*W^4/(Cg^2*Vch(1)^2));
error_mob2=-delta(2)*W^4/(2*Cg^2*Vd*Vch(1)^2);
error_mob= [error_mob;(error_mob1+error_mob2)/2];
error_n0=[error_n0;(sqrt(delta(3)*W^2/(e^2*mob^2*Lds^2*Vch(1)^2)))];

%
disp (strcat('File #',num2str(k-2),'___', nom));
disp (Vd);
disp(mob1);
disp(mob2);
disp(n0);

end

figure
%plot(fin1(:,1),fin1(:,2),'o')
errorbar(fin1(:,1),fin1(:,2)*1E+4,error_mob*1E+4,'o')
xlabel('nombre de passages')
ylabel('mobilité (cm^2.v^-^1.s^-^1)')
figure
%plot(fin2(:,1),fin2(:,2),'o')
errorbar(fin2(:,1),fin2(:,2)*1E-4,error_n0*1E-4,'o')
xlabel('nombre de passages')
ylabel('n_0 (cm^-^2)')
figure
plot(fin3(:,1),fin3(:,2),'o')
xlabel('nombre de passages')
ylabel('V_D (V)')
```

III. Organization on the time passed on each lab

- 11 months in IEMN: growth and transfer of graphene. First transfer of h-BN provided by CINTRA. Study of printed transistors.
- 6 months in CINTRA: growth of h-BN, growth of 3DC and 3DBN. Fabrication of 1st generation substrates, growth of single crystals graphene.
- 4 months in IEMN: characterization of substrate of 1st generation, transfer of graphene by bubbling technique.
- 8 months in CINTRA: growth of h-BN, growth of 3DBN and 3DC, fabrication of substrates of 2nd generation.
- 9 months in Lille: transfer of h-BN by two methods, characterization of substrates of 2nd generation.